T2 Characterization of Oil-In-Water Emulsions for NMR Sensor Applications

By

Alexa S. Zammit

B.S. Chemical Engineering, United States Military Academy, 2022

Submitted to the Department of Materials Science and Engineering in partial fulfillment of the requirements for the degree of

MASTER OF SCIENCE IN MATERIALS SCIENCE AND ENGINEERING

at the

MASSACHUSETTS INSTITUTE OF TECHNOLOGY

February 2024

© 2024 Alexa S. Zammit. All rights reserved.

The author hereby grants MIT a nonexclusive, worldwide, irrevocable, royalty-free license to exercise any and all rights under copyright, including to reproduce, preserve, distribute, and publicly display copies of the thesis, or release the thesis under an open-access license.

Authored by: Alexa S. Zammit
Department of Materials Science and Engineering
January 19th, 2024

Certified by: Michael J. Cima
Professor of Materials Science and Engineering
Thesis Supervisor

Accepted by: Robert J. Macfarlane
Professor of Materials Science and Engineering
Chair, Department Committee on Graduate Studies

T2 Characterization of Oil-In-Water Emulsions for NMR Sensor Applications

By

Alexa S. Zammit

Submitted to the Department of Materials Science and Engineering in partial fulfillment of the requirements for the degree of

MASTER OF SCIENCE IN MATERIALS SCIENCE AND ENGINEERING

ABSTRACT

Fluid status assessment is an essential aspect of healthcare with implications in chronic conditions such as renal disease and congestive heart failure. Current fluid status determination techniques lack quantitative methods and standards. Our research explores a point-of-care approach through a portable single-sided magnetic resonance (MR) sensor. We are developing a more accurate and clinically relevant hydration metric through measuring localized skeletal muscle. Phantoms are used as stand-ins for a human subject to calibrate and ensure system functionality. The microstructure of an emulsion also mimics the multiple compartments of tissue such as the intra and extracellular volumes of muscle and adipose tissue. We aim to use oil-in-water emulsions as phantoms to ensure device reproducibility and determine how much the scale of the microstructure affects relaxation behavior. A quantitative understanding of the length scales appropriate for muscle and adipose tissue will help determine the reliability of our hydration measurement.

Thesis supervisor: Michael J. Cima
Title: Professor of Materials Science and Engineering

Acknowledgements

I would like to first and foremost acknowledge and thank my advisor, Professor Michael Cima. He taught me how it is important to keep the bigger picture of the project in mind while focusing on specifics to ensure that both the academic and application-oriented goals of the project are met. Thank you to Wendy Brown and all the members of the Cima Lab. Wendy is always there for us to provide insight with almost anything we might have trouble with and always willing to help. I am very appreciative of all of the members of the lab, past and present, who are always there to answer questions, talk through issues, or grab a coffee. Although our time in the lab never overlapped, I am grateful that Dr. Ashvin Bashyam, Dr. Chris Frangieh, and Dr. Lina Colucci would make time to answer questions about their work on the MR project. Furthermore, I would like to thank our collaborators at Massachusetts General Hospital for working with us on the MR project and enabling our work with dialysis patients. Thank you to the National Institutes of Health for the funding on our project and the National Science Foundation for the Graduate Research Fellowship. I am immensely grateful for Dr. Jeffrey Kuhn and Jeff Wyckoff in the Koch Institute Microscopy Core facility, who guided me and enabled me to find the optimal way to see my project on a different scale. Additionally, Mike Tarkanian provided a lot of assistance and information regarding what DMSE resources were available to us.

I am incredibly grateful for all my wonderful friends and classmates in my cohort. Our many late nights studying together and spending time together outside of the classroom are memories that I will always look fondly on. The professors of my courses broadened my knowledge of materials science and expanded my understanding of how fundamental concepts are applied to some of the most complex topics to better comprehend different aspects of the field.

Thank you to my professors and mentors at the United States Military Academy. COL John Burpo was my undergraduate research advisor who fostered my passion for research. Both COLs Burpo and Melnyk continue to support me beyond my graduation from USMA.

Thank you to my parents, friends, and family for being my support system. Thank you to Hannah for supporting me and being a source of comfort throughout the ups and downs of earning my master's degree. Thank you to my parents, Helena and Michael; my sisters, Victoria and Gabrielle; and my brother, John. I also extend my gratitude to my cousins, aunts, uncles, and grandparents. Your unwavering support and encouragement have been invaluable. I love you all dearly, and this achievement is ours, equally.

Contents

List of Figures

List of Tables

Chapter 1

Introduction

1.1: Fluid Management Problem – Existing Methods

Hydration status and fluid management are important components of medical care in a variety of clinical settings[1]. Adequate fluid intake and being well hydrated are closely linked to optimal gastrointestinal, kidney, and heart function. Fluid management is also a key contributing factor to the progression of chronic conditions such as congestive heart failure and renal disease[2], [3]. Both hypervolemic (fluid overloaded) or hypovolemic (fluid underloaded) states are detrimental to patient health. There is currently no accepted method for assessing hydration status or agreement on a "gold standard" for fluid status determination; despite the importance of such a metric[1]. Qualitative metrics and symptoms of dehydration such as decreased skin turgor, dry oral mucosa, or urine color are generally used, but have poor sensitivity and specificity[4]. These symptoms are not typically apparent unless patients are moderately dehydrated or worse. The lack of both a qualitative and quantitative standard to detect fluid status creates a gap that many try to address[5], [6], [7], [8].

Current methods of hydration status determination range between fluid analysis within a specific compartment to a systemic measurement. Fluid is largely stored in two compartments within the body: the intracellular and extracellular spaces [9], [10], [11]. These compartments exist throughout the body throughout both muscle and adipose tissue. The changes in fluid between these compartments do not occur equally. Each compartment contributes to the overall fluid

status throughout the body. Lean muscle consists of around 75% water[12]. Changes in fluid volume in the extracellular compartment of the muscle are direct reflections of hypovolemic or hypervolemic states[13]. Existing assessments to measure fluid in specific locations and compartments through tests using blood, saliva, and urine[9]. These compartmental assessments take time to acquire results and contain confounding variables. Tests such as urine color require several considerations to avoid the influence of confounding factors. Samples reflect all of the fluid in the bladder since the previous void and ingested fluids can be excreted before the intracellular and extracellular fluid equilibrate within the body[9], [10], [14], [15].

Existing methods for determining systemic hydration status include bioimpedance, body mass, vital signs and sensations of thirst, dual-energy x-ray absorptiometry, and neutron activation analysis[10]. Bioimpedance provides a method for low cost, portable, noninvasive body composition assessment by estimating total body water, and other composition metrics, through measuring the resistance to the flow of electrical current throughout the body[16], [17]. Bioimpedance devices are more frequent in the clinic as more research is conducted[7], [8], [18], [19], [20]. Clinical accuracy of bioimpedance devices depends on limiting factors due to variations in body composition, amount of subcutaneous fat, and the inability to make a distinction between the extracellular and intracellular compartments[18]. Changes in body mass can be used to estimate changes in total body water through volume of water lost as long as confounding variables such as fluid/food consumption, excretion, sweat composition, time of day, and respiratory water loss are accounted for[10]. Even when these factors are accounted for, a change in body mass can only provide changes relative to the initial hydration status and cannot precisely measure hydration status. Changes in vital signs and sensations of thirst are indicative of a dehydrated state. These symptoms are subtle and may be unreliable; and are

dependent on patient age as older adults exhibit decreased thirst sensation [21], [22]. Neutron activation analysis consists of exposing a patient to a neutron field and measuring the total body chloride, potassium, and sodium using radiation detectors to determine intracellular and extracellular volume[9], [10], [23]. The scans measure total body water with some accuracy; however, a scan typically takes one hour to complete, requires use of costly equipment, requires exposing a patient to radiation, and requires technical expertise to conduct[10].

1.2: Our Lab's Device

The Cima Lab suggests that a localized skeletal muscle measurement using a portable magnetic resonance (MR) sensor can acquire a clinically relevant and quantitative metric of hydration state based on preliminary studies[24], [25], [26], [27]. It uses two MR devices, one that was built by Matthew Li and one that was built by Sydney Sherman. The MR sensors are designed with permanent rare earth magnets to have a static B0 field. Both contain a magnet array similar to the unilateral linear Halbach design that is demonstrated in Figure 1-1.

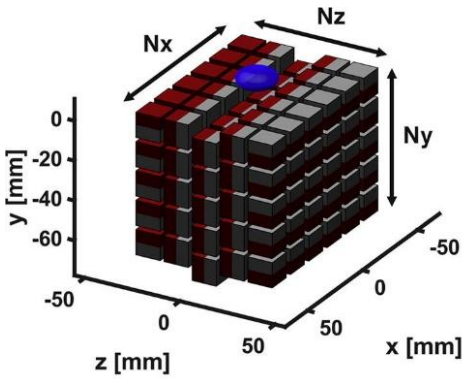

Figure 1-1. Unilateral Linear Halbach concept with sensitive area in blue[26].

This design is ideal for a clinical setting because it focuses the field on one side of the device. Focusing the field eliminates the effects of stray fields on the other faces of the magnet. Each

sensor contains a radiofrequency (RF) surface coil and impedance matching network. The sensors use a Kea2 Spectrometer (Magritek, Wellington, New Zealand) to acquire signal. Prospa software (Magritek, Wellington, New Zealand) provides the setup and analysis interface. The internal spectrometer RF amplifier is connected via coaxial cable to the matching network[27]. Car-Purcell-Meiboom-Gill (CPMG) pulse sequence to capture T2 relaxation data for analysis. T2 relaxation, also known as transverse or spin-spin relaxation, measures the dephasing of spinning dipoles in the transverse plane. The Sherman sensor (Figure 1-2) was built after the Li sensor to incorporate design changes based off of the results from an initial clinical study[25]. Data collected from the Li sensor was compared to MRI results on dialysis patients before and after dialysis. The Sherman sensor was developed after the need for a more homogeneous field and sensitive area with a greater depth arose.

The use of a permanent magnet array in the devices and RF coil enables a minimized overall cost to produce the device as well as low energy consumption during use. The magnetic field profiles of both the Li and Sherman sensors are shown in Figure 1-2 below. Both magnets contain specified homogeneous regions with field gradients that decrease in strength as the distance from the homogeneous region increases.

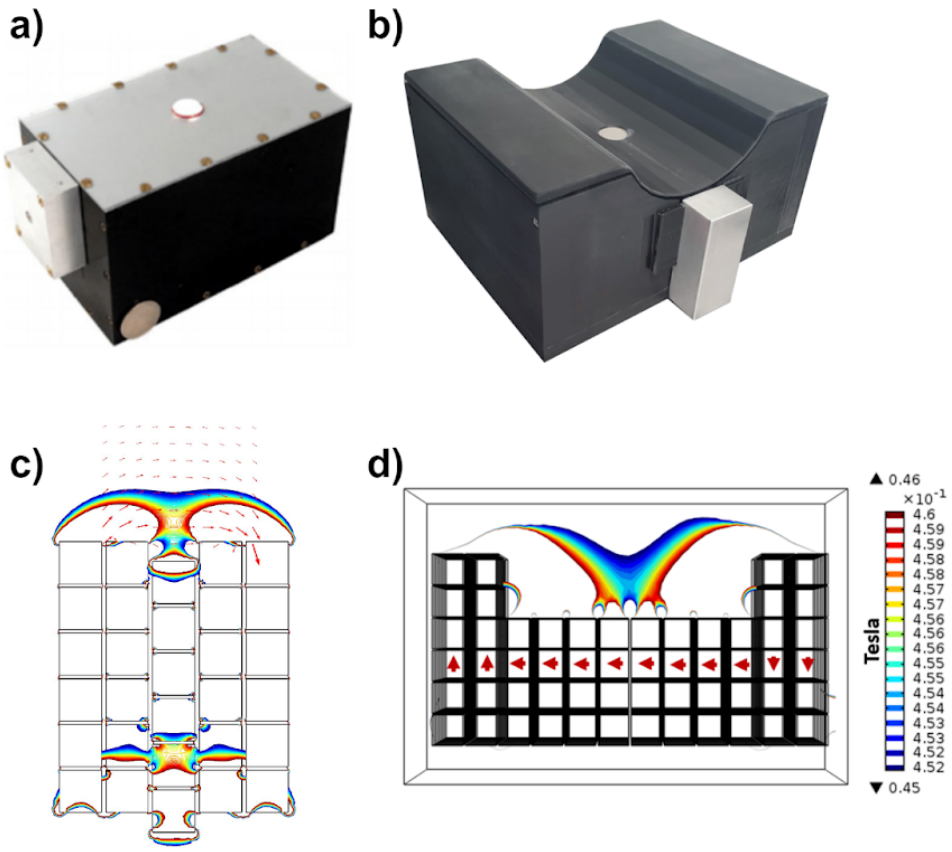

Figure 1-2. Images of a) the Li sensor and b) the Sherman sensor. COMSOL simulations of magnetic field profiles for c) the Li sensor and d) the Sherman sensor. Arrows indicate the field orientation[27].

The main difference between the sensors is that the most homogeneous region, or "sweet spot", on the magnet sits at a greater depth in the Sherman sensor. The greater depth was needed to ensure that the device is collecting data from the skeletal muscle rather than subcutaneous adipose tissue. This is because the desired metric to collect with the sensor is the fluid status of the extracellular component in skeletal muscle as it is a reflection of systemic fluid status.

The two sensors contain different field strengths and gradients. The magnetic field strength dictates what RF frequency is needed to flip with spins of the protons when using the CPMG pulse sequence. The field gradient enables the ability to specify a frequency that corresponds to a

desired measurement volume above the surface of the RF coil. Pulse frequency is set to the corresponding height to measure within the sweet spot of each device to maximize the signal collected. One drawback of a fixed magnetic field gradient is that protons in different areas of the field gradient will have different relaxation behavior. The Li sensor sweet spot is between 2-3mm above the surface of the RF coil. Colucci found that the sweet spot of their sensor was measuring both muscle and subcutaneous tissue in an initial clinical study on fluid assessment in dialysis patients[25]. Sherman designed a new sensor with a sweet spot that is 8mm above the surface of the magnet when designing and building an updated sensor for this reason[27]. The sweet spot at a greater depth above the surface of the RF coil on the Sherman sensor aims to only measure skeletal muscle.

The benefit to collecting data only in the muscle tissue is that the data can be fit to a biexponential fit where the individual peaks of the biexponential fit are the reflections of the distinct intracellular and extracellular fluid compartments. This method of using a biexponential fit on muscle tissue was determined by analyzing the pixel-wise relaxation values from MRI results of study participants [25].

$$y(t,\ A,\ \tau) = \sum A_n * e^{-t/\tau_n} \tag{1-1}$$

The multiexponential T2 decay curve uses Equation 1-1 to find the individual relaxation times and amplitude components of each compartment where A is the amplitude of the exponential peak, and the corresponding τ is the relaxation time constant of that peak. y is the amplitude of the raw decay signal in microvolts (μV) and t is the time of the raw signal acquisition in milliseconds (ms).

1.3: Clinical Applications of the device

Currently the Sherman sensor is used in an ongoing clinical study. The clinical study (MGH IRB# 2022P002140) team is working with dialysis patients to scan a patient's calf muscle before and after dialysis. The aim of this study is to show that it is possible to use the device as a point-of-care diagnostic tool to determine patient hydration status.

There are many different factors that impact the quality of the data when collecting data using an MR sensor on a human subject. The data quality is best quantified using the signal to noise ratio (SNR), which divides the initial signal amplitude by the standard deviation of the noise. Higher SNR means that the confidence in the data and the resulting multiexponential fit is higher. The data is noisier at a lower SNR. This results in lower confidence in the exponential fit. There are many different factors that impact the SNR during data collection. Methods such as plugging the spectrometer into an in-line filter and grounding the subject help to reduce extraneous noise. Encasing the impedance matching network in aluminum and confirming contact between the subject, matching network, and grounded aluminum base plate are also essential steps in ensuring noise minimization. A proper ground between the aluminum base plate and the sensor is important. Ensuring a proper connection between the spectrometer and aluminum plate via a grounding wire is paramount. There are still many ways to reduce noise despite the methods already used. Each data collection environment is different and influenced by other devices plugged in the vicinity. Other equipment operating nearby (ie: the same area, could be on a different floor) can impact the noise picked up by the sensor.

1.4: Emulsions

Both qualitative and quantitative phantoms are used as stand-ins for human tissue to ensure that the system and methods are functioning correctly in MRIs[28]. Qualitative phantoms have visually similar physical attributes to humans and confirm imaging capability. Quantitative phantoms do not appear to have human attributes as only the signal collected by the MRI is required to mimic that of a human subject. A cost-effective, stable, repeatable, and reproducible phantom is needed due to the experimental nature of the MR sensors in the Cima Lab. Previous studies explore using emulsions and gels as phantoms for MR applications[29], [30], [31]. Emulsions are desirable and often used as quantitative phantoms because the dual component nature enables a two-compartment MR-based quantification measurement[32], [33], [34], [35], [36]. Emulsions consist of a continuous and dispersed phase of two otherwise immiscible fluids. Often these phases consist of oil and water. The relaxation behavior of the dispersed oil phase is largely dependent on two kinds of diffusivity. The first is the diffusion of protons within the oil droplets that is independent of droplet size[37]. The second kind of diffusion is based on the diffusion of the oil droplets due to Brownian motion. A higher concentration of oil droplets restricts diffusion and results in longer relaxation times as the Brownian motion of the droplets is more restricted [37]. The emulsions contain agar in the aqueous phase to suspend the oil droplets in a gel. This suspension of the oil droplets helps prevent diffusion of the oil droplets due to Brownian motion. Preventing diffusion of the oil droplets is important because it further simplifies the system and better mimics the behavior of human tissue.

The Cima Lab adopted the protocol from Bush et. al, but does not include using gadolinium-diethylenetriaminepentacetate (DTPA) contrast agent[24], [27], [29]. Peanut oil was chosen for the oil phase because the triglycerides contain similar relaxation properties to human

subcutaneous adipose tissue since the Sherman and Li sensors collect T2 relaxometry data. We hypothesize that each peak in the multiexponential fit is a superposition of the individual fits that result from the dispersed and continuous phases when fitting the T2 data collected from an emulsion. This is similar to collecting data on a human subject where anticipated fitted peaks are reflective of the intracellular and extracellular environments. This thesis explores the hypothesis of the superposition of the individual components of the emulsions and characterizes the microstructure of the emulsions. The difference between microstructure scale and corresponding relaxation properties was also explored. These results are compiled and presented along with suggestions for future work.

Chapter 2

T2 Characterization of Emulsions

2.1: Background

The protocol adopted from Bush et al. is different from other oil-in-water emulsions used as phantoms for MR purposes. This is because agar is added in the aqueous phase which gels upon cooling[29]. Adding agar effectively makes the emulsions oil-in-gel rather than oil-in-water. This distinction is important because the agar effectively suspends the oil droplets in a gel matrix. Preventing the oil droplets from moving prevents the droplets from diffusing because of Brownian motion. The intracellular and extracellular compartments of muscle tissue are relatively fixed compared to an oil-in-water emulsion. This means using agar to similarly fix the oil droplets creates an oil-in-gel emulsion that makes the samples more representative of muscle. Controlling the oil volume fraction of the emulsions enables the ability to additionally mimic adipose tissue.

2.1.2: Hypothesis

Each exponent in the fit is a superposition of the individual components in a multiexponential fit used for human subject and emulsion data. The exponential fit of an emulsion should consist of three exponents: two for the dispersed phase of peanut oil droplets and one for the continuous phase, which consists of an aqueous solution gelled with agar. We anticipate the relaxation times of the dispersed and continuous phases to stay constant and the amplitudes to fluctuate as the oil

volume fraction of the dispersed phase changes. The characteristics of the microstructure within the emulsions will be explored. We also aim to explore if changing the characteristics of the microstructure results in changes to the relaxation properties of the emulsions.

2.2: Methods and Materials

The aqueous and oil phases are first made separately to prepare the emulsions. The desired amount and oil volume fraction of the emulsion are calculated. 35 mL of the aqueous phase and 15 mL of the oil phase are required to create a 50 mL batch of 30% oil volume emulsions. The emulsions were fabricated according to the general protocol described in Bush et al.[29] and modified as described in Sherman et al[27]. It is important to note that the amount of aqueous phase prepared should be at least 10 mL larger than the desired volume. This is to account for a test that requires removing 2 mL of the aqueous phase from the bulk solution. The rest of the additional volume is to account for evaporation of the aqueous phase. The amount of aqueous phase that evaporates depends on the volume of the bulk solution where a larger batch experiences a smaller amount of evaporation by volume percent. A 50mL batch of aqueous phase is prepared despite only needing 35 mL of the aqueous phase to create a 50 mL batch of 30% oil volume emulsions. This is to ensure that there will be a sufficient volume of aqueous phase available after evaporation during production and testing for gel stability.

The aqueous phase is created by first measuring the desired amount of deionized water. To prepare a 50 mL aqueous phase, 50 mL of deionized water is first added to a 150mL beaker with a stir bar on a hot plate to continue from the example above. Set the temperature to 90°C and a slow stir rate around 100rpm. Next measure 0.05g sodium benzoate and add it into the beaker.

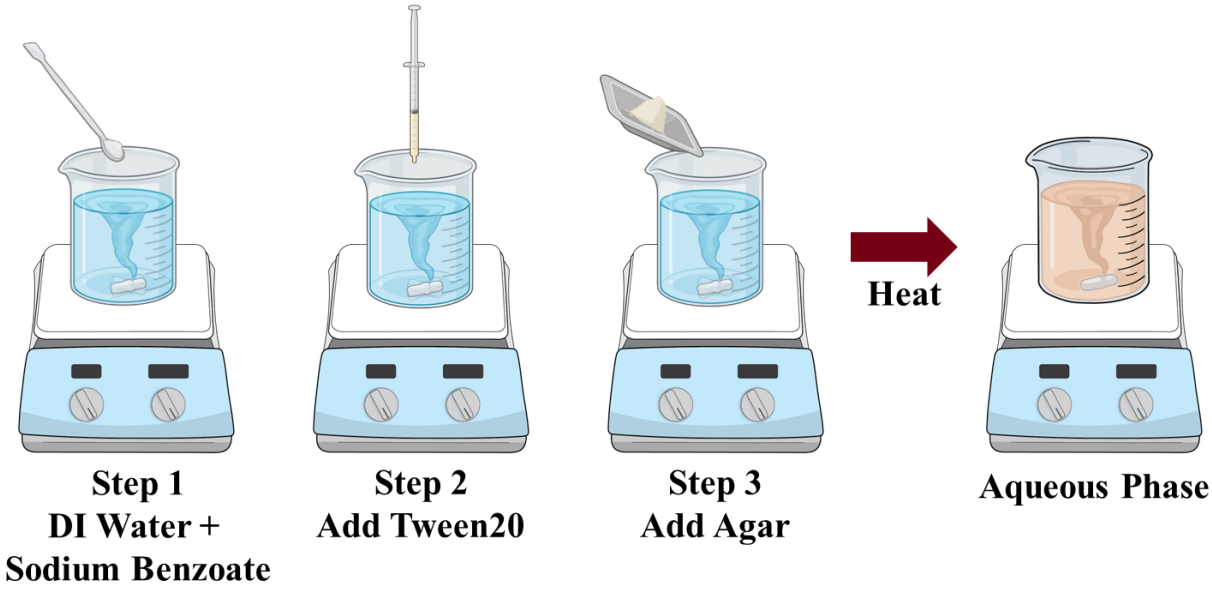

Figure 2-1. Illustration of Aqueous Phase Preparation.

Ensure that the beaker is covered using aluminum foil to minimize evaporation. Add 0.1 mL of tween 20 and increase the stir rate to 500rpm. Add 1.5g of agar slowly into the beaker last. Once complete, increase the temperature to 180°C and a stir rate of 800 rpm for ten minutes. Figure 2-1 outlines the individual steps in preparing the aqueous phase. It is important to make sure that there are no air bubbles caused by the high stir rate, as it can prevent the oil from emulsifying. Mixing of the aqueous phase is complete when the solution is clear with an amber color and no air bubbles, clumps, or streams of agar. Place at least 2 mL of the aqueous solution into a glass scintillation vial to test that the aqueous solution will set. The aqueous phase will set and should be completely firm and become opaque upon cooling. Continue mixing the aqueous phase at 180°C if the agar does not set. Lower the heat on the hot plate to 90°C if the agar sets. Lower the temperature of the hot plate if the aqueous phase shows signs of boiling (typically a stream of bubbles) at any time.

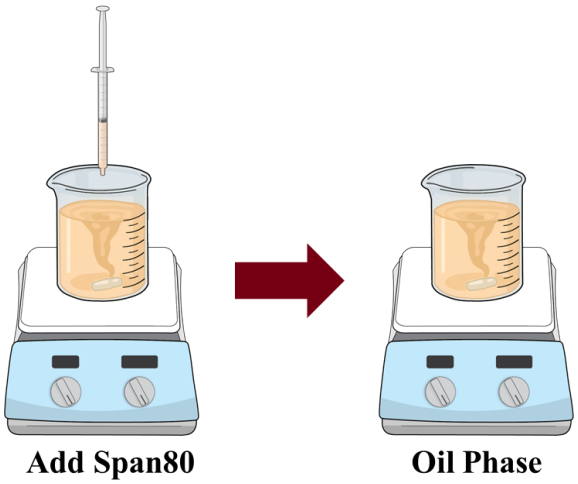

Figure 2-2. Illustration of Oil Phase Preparation.

The oil phase is prepared simultaneously while the aqueous solution is mixing. An additional 5 mL of oil phase is prepared to ensure there is enough stock to make the emulsion similar to the aqueous phase. 20 mL of peanut oil is added into a clean beaker with a stir bar on a hot plate to continue from the example above. Set the temperature to 150°C and a stir rate of 700 rpm. Add in 0.2 mL of span 80 and mix for five minutes. Ensure that the oil phase is monitored during heating. Decrease the temperature of the hot plate if the oil begins to smoke. Lower the temperature of the hot plate to 100°C after five minutes of mixing.

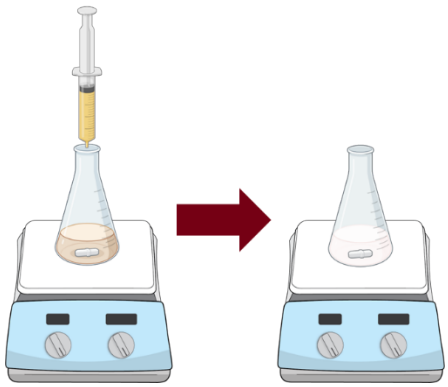

Figure 2-3. Emulsion Preparation Illustration.

Prepare the emulsion by first weighing the Erlenmeyer flask and stir bar. Then add the desired amount of water phase into the flask according to the desired final emulsion oil volume

component. Add 35 mL of the aqueous phase into a 125 mL Erlenmeyer flask according to the example above. Weigh the combined total of the aqueous phase, Erlenmeyer flask, and stir bar. Set the hot plate to 95°C and the beginning stir rate should be around 200 rpm. This mixing rate may vary depending on the volume of aqueous phase and the size of the Erlenmeyer flask. The stir rate should not be fast enough to introduce air bubbles into the mixture. This is similar to the preparation and mixing of the aqueous phase. Slowly add in the oil phase solution dropwise. At oil volume fractions above 35%, the oil should not be added faster than 1 drop per second. Increase the stir rate as the emulsion volume increases. Increase the stir rate to 700 rpm after 5mL of the oil phase is added. This incremental increase is necessary to ensure that air bubbles are not inadvertently incorporated into the emulsion. Air bubbles will cause the emulsion to phase separate before reaching high percentage oil volume fractions. The emulsion is stirred at 1100 rpm for an additional 10 minutes once the oil phase is completely added.

The emulsion is completely mixed when there is no visible oil (either in the form of streaks or droplets) and is white with a smooth texture. Weigh the combined total of the aqueous phase, oil phase, Erlenmeyer flask, and stir bar once the emulsion is completed. The weight of the aqueous phase is determined by subtracting the weight of the flask and the stir bar from the weight of the beaker when it contains only the aqueous phase. The weight of the oil phase is determined by subtracting the weight of the flask and aqueous phase from the weight of the completed emulsion. These weights are used, as demonstrated in Equations 2-1 through 2-3, to determine the oil volume percent for each batch of emulsions. The oil volume percent determined by weight is typically within one percent of the targeted oil volume. The emulsions are referred to by their targeted oil volume percent for simplification.

$$W_{aq.} * \frac{1\ mL}{0.998g} = V_{aq.} \tag{2-1}$$

$$W_{oil} * \frac{1\ mL}{0.912g} = V_{oil} \quad (2\text{-}2)$$

$$\%\ Oil\ Vol. = \frac{V_{oil}}{V_{oil} + V_{aq}} * 100\% \quad (2\text{-}3)$$

The emulsion is then transferred into either a scintillation vial for data collection or a microscope slide for imaging. Nile red (Millipore Sigma) is a lipophilic stain used to dye the oil phase for fluorescent imaging. Nile red was purchased as a powder. A 1mM stock solution of nile red was created by dissolving the powder into acetone. This stock solution was contained in an amber bottle that was also wrapped in aluminum foil to minimize the risk of photobleaching and maintain dye potency. The dye is added to the emulsion after the oil phase is completely added but before the 10 minutes of mixing. 3 µL of the 1mM nile red stock solution were added for every 1 mL of oil added. The emulsion will have a pink tint and should not have streaks of a darker pink or red when completely mixed with the dye. The microscope slide is prepared by creating a square of four strips of double-sided tape on the slide. The slide is then pre-warmed on a hot plate at 100°C.

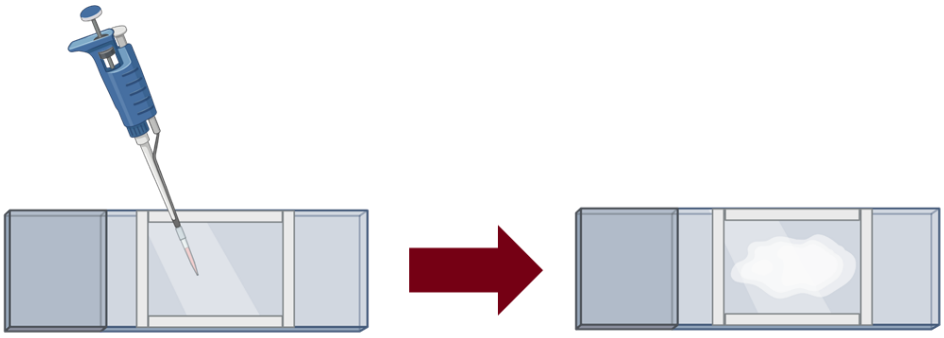

Figure 2-4. Microscope Slide Preparation Illustration.

Pipette approximately 100 microliters of the emulsion into the square on the microscope slide using a micropipette. A coverslip is lightly placed over the sample immediately after the emulsion is loaded. The weight of the coverslip gently spreads the unset emulsion enough until it

contacts the double-sided tape. Clear nail polish can seal and contain the sample if the emulsion spreads beyond the edges of the double-sided tape. The microscope slides are stored in a refrigerator at 4°C once the agar gels and the emulsion sets on the benchtop.

2.3: Data Acquisition and Processing

The T2 relaxometry data on the Li sensor is acquired using a B1 frequency of 11.66MHz, 8192 echoes, an inter-experimental delay of 600 milliseconds, a 90 degree amplitude of -12dB, a 180 degree amplitude of -6dB, a pulse length of 12 microseconds, and an echo time of 65 microseconds, with one dummy echo. The signal acquisition consists of 16 scans that are completed with 16 complex points and a dwell time of 0.5 microseconds. The Sherman sensor operates under similar acquisition parameters. Key differences are that the Sherman sensor uses a B1 frequency of 8.38MHz, a 90 degree amplitude of -6.5dB, a 180 degree amplitude of -0.5dB, and an echo time of 80 microseconds. One run of 16 scans takes approximately one minute to complete. In total, ten runs of 16 scans are collected for one set of data.

2.3.1: Relaxation of Individual Components

The T2 relaxation of the individual components of the emulsion are depicted in Figure 2-5. The exponential decay curve of the two phases are visibly different. This indicates that the number of exponents in the two curves are different. We determined that the aqueous phase consists of a monoexponential fit and the oil phase consists of a biexponential fit. This was determined by fitting the relaxation profiles to monoexponential, biexponential and a triexponential fit. Minimal error and a high R^2 made it apparent that the aqueous phase follows a monoexponential fit while

the oil phase follows a biexponential fit. Too many parameters and overfitting were evident when one or more peaks contained a low relative amplitude or contained identical peaks. The relative amplitude of the second peak was less than 5% of the total amplitude when the aqueous phase was incorrectly fit to a biexponential. The relative amplitude of the third peak exhibited similar behavior when the oil phase was incorrectly fit to a triexponential equation. The resulting relaxation times from overfit data was also wildly inconsistent for near-identical samples and further confirmed that the data was over-fitted.

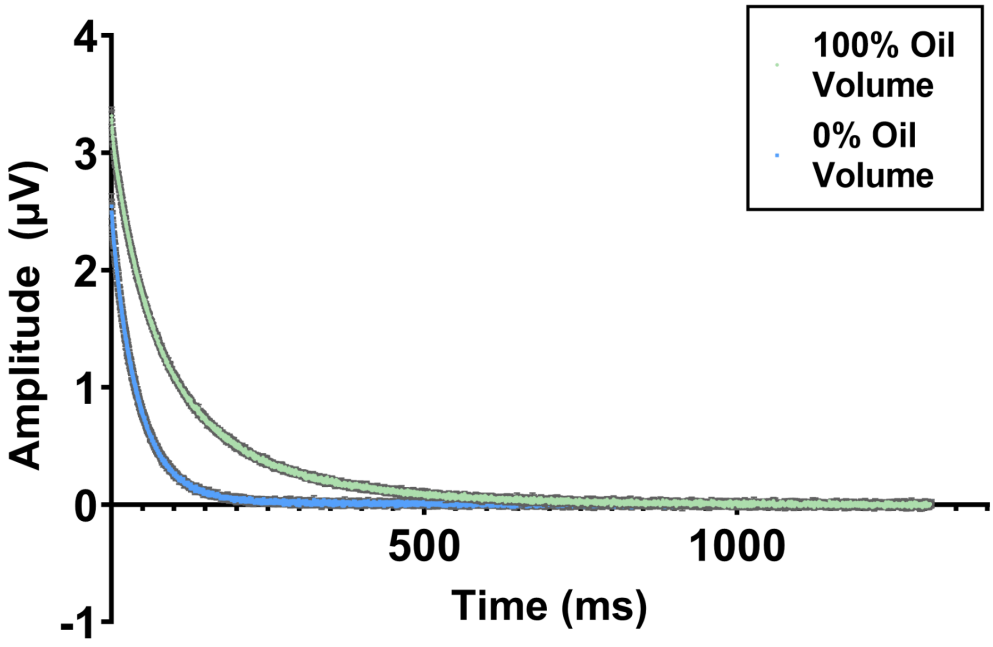

Figure 2-5. Raw T2 Relaxometry Data of Individual Aqueous and Oil Phases.

A theoretical analysis of the protons present in each phase additionally confirmed the monoexponential fit of the aqueous phase and biexponential fit of the oil phase. The aqueous phase primarily contains protons present in water and supports the observation of a monoexponential fit. The oil phase contains two different kinds of protons. We examined the different protons within triglycerides as they are a main component of peanut oil. Triglycerides contain protons on both the polar and nonpolar sides of the molecule. These protons exhibit

different relaxation profiles because of the polarity in the molecule. This explains why a biexponential fit is necessary for peanut oil. Peanut oil and corn oil are similar in composition of triglycerides. Previous studies also examined and concluded that corn oil requires a biexponential fit[38], [39]. We expect the emulsions to have a triexponential fit as a superposition of the monoexponential and biexponential components.

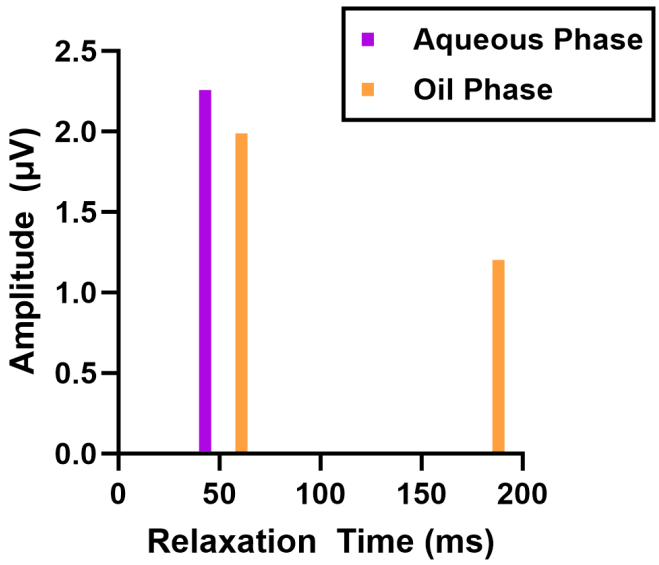

Figure 2-6. Superimposed Fit Results of the Aqueous and Oil Phases.

Figure 2-6 graphically depicts the superimposed fit results of the amplitudes and relaxation times of the monoexponential aqueous and biexponential oil phases. From lowest and fastest relaxation time to highest and longest relaxation time, each peak will be labeled numerically. The peak with the lowest relaxation time from a triexponential fit will be referred to as “peak 1.” The middle peak will be labeled as “peak 2” and the highest relaxation time will be referred to as “peak 3.” The relaxation times of the aqueous phase and the shorter relaxation time of the oil phase are within 15 milliseconds of each other. This can result in difficulty of fit determination and especially for a triexponential fit with six parameters.

2.3.2: Data Processing Pipeline

The Li sensor was primarily used for this study of characterization of the emulsions even though the Sherman sensor is the main device used by the Cima Lab. This is because during this time, the Sherman sensor was involved in the previously mentioned clinical study (MGH IRB# 2022P002140). The differences in signal amplitude and sensitivity to noise on the two sensors impact the resulting fitted relaxation times. This was characterized by measuring various concentrations (0.001M – 0.2M) of copper sulfate ($CuSO_4$) on both sensors. $CuSO_4$ can be characterized with a monoexponential fit and diluting these solutions with water increases the relaxation time. This difference is depicted in Figure 2-7 and closely follows a quadratic relationship between the two sensors. The relaxation times that result from the Li sensor are faster than the relaxation times that result from the Sherman sensor. This is expected because the gradient of the Li sensor is much larger than the gradient in the Sherman sensor.

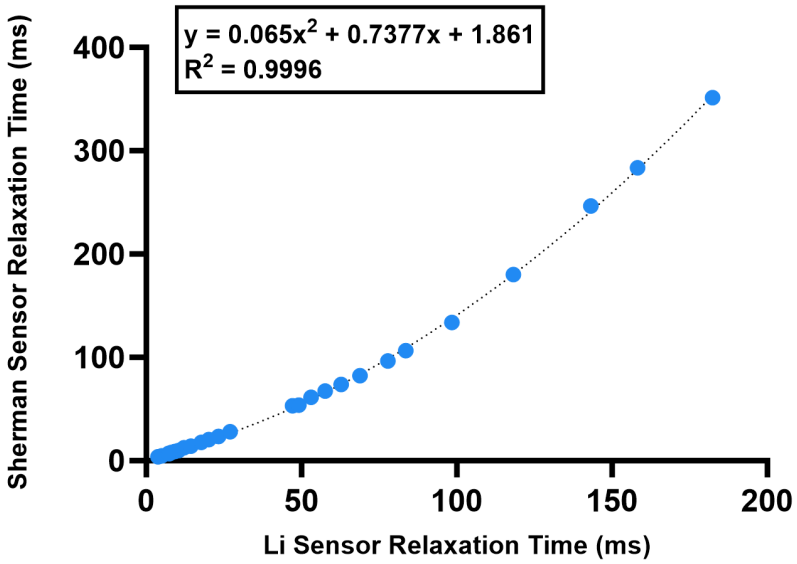

Figure 2-7. Comparison of T2 Relaxation Time Outputs from Sherman and Li Sensors[27].

Raw T2 relaxometry data requires processing to get as accurate of a fit as possible. Figure 2-8 below shows an example of a raw, single CPMG pulse sequence recorded in a minute-long acquisition.

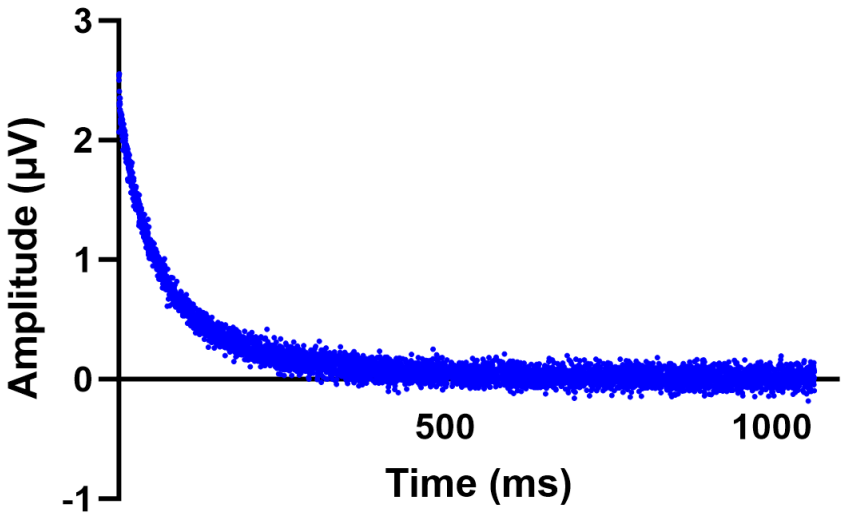

Figure 2-8. Raw T2 Relaxometry Data of a 50% Oil Volume Emulsion.

10 CPMG acquisitions are run through a quality control to process one set of data. For each minute-long acquisition, the first 3 points are removed. Next, the first 3 of the remaining points are averaged to determine the y-intercept. The amplitude of the tail is determined by averaging the last 1000 points from the scan. The offset is calculated by finding the difference between this average and zero. The acquisition is then offset corrected by adjusting the amplitude of the entire dataset by the offset factor. Next, the total area, cumulative area, and SNR are determined for each acquisition. Each individual acquisition is compared to the others by determining outliers among the 10 acquisitions. These outliers are determined by quartiles and compare the y-intercepts, total areas, and cumulative areas of each acquisition. The MATLAB code recommends eliminating runs that contain values that are more than 1.5*IQR (interquartile range) above the upper quartile (75%) and below the lower quartile (25%). Additionally, runs are

suggested to be eliminated if it contains a value lower than the threshold SNR or y-intercept values. The threshold SNR is 5, and the threshold y-intercept is a signal amplitude of 1.4 μV. The quality control code then averages all of the scans, regardless of recommended removal, and separately averages only the recommended scans that meet the inclusion criteria.

The data can then be fit to a triexponential fit after the quality control is performed. This is done by first reading in the desired dataset. The dataset is then run through a function that conducts three separate triexponential fits using different methods to compare the results. The different fitting methods consist of a global search algorithm, genetic algorithm, and nonlinear least squares fit. The global search uses a function to find the minimum of a constrained nonlinear multivariable function (fmincon). The genetic algorithm begins with an initial guess and iteratively searches for a minimum until one is found, or the maximum number of generations is reached. The nonlinear least squares fit uses a least squares curve fit to determine the variables of the triexponential function.

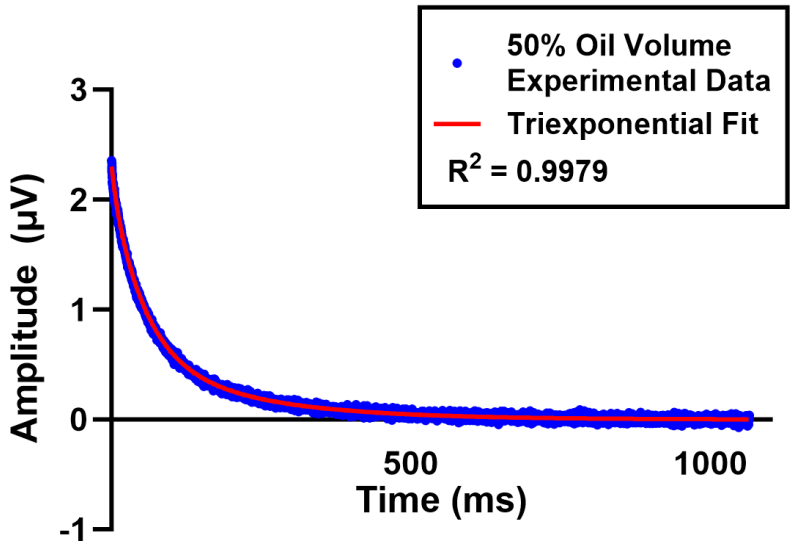

Figure 2-9. Processed and averaged T2 Relaxometry Data of a 50% Oil Volume Emulsion.

Figure 2-9 shows the results from 10 CPMG acquisitions processed and averaged in blue. The triexponential fit of the processed data is shown in red.

$$y = A_1 * e^{a*t} + A_2 * e^{b*t} + A_3 * e^{c*t} \quad (2\text{-}4)$$

Equation 2-4 is the format in which the code produces the coefficients of the triexponential fit. This equation is an expansion of Equation 1-1. To determine the values of the relaxation time constants, the negative reciprocal of a, b, and c are calculated to determine coefficients $\tau_{2,1}$, $\tau_{2,2}$ and $\tau_{2,3}$. The same calculation is completed to obtain the confidence interval values for each of the six parameters.

2.4: Individual Component Superposition

The raw experimental data was compared to a synthetic dataset to test whether the experimental relaxation data of the emulsions were a superposition of the individual components. The synthetic dataset was created using a volume-weighted average of the oil component as demonstrated in Equation 2-2.

$$y = (1 - \varphi)A_1^0 * e^{-t/\tau_{2,1}^0} + \varphi * (A_2^0 * e^{-t/\tau_{2,2}^0} + A_3^0 * e^{-t/\tau_{2,3}^0}) \quad (2\text{-}5)$$

Confirmation of a superposition of the individual components required an equation that includes the results of the monoexponential fit from the aqueous phase and the biexponential fit from the oil phase. φ is the oil fraction of the emulsion, A_1^0 and $\tau_{2,1}^0$ are the amplitude and relaxation time determined from the monoexponential fit of the aqueous phase, and A_2^0, $\tau_{2,2}^0$, A_3^0, and $\tau_{2,3}^0$ are the

amplitudes and relaxation times that result from the biexponential fit of the oil phase for this reason.

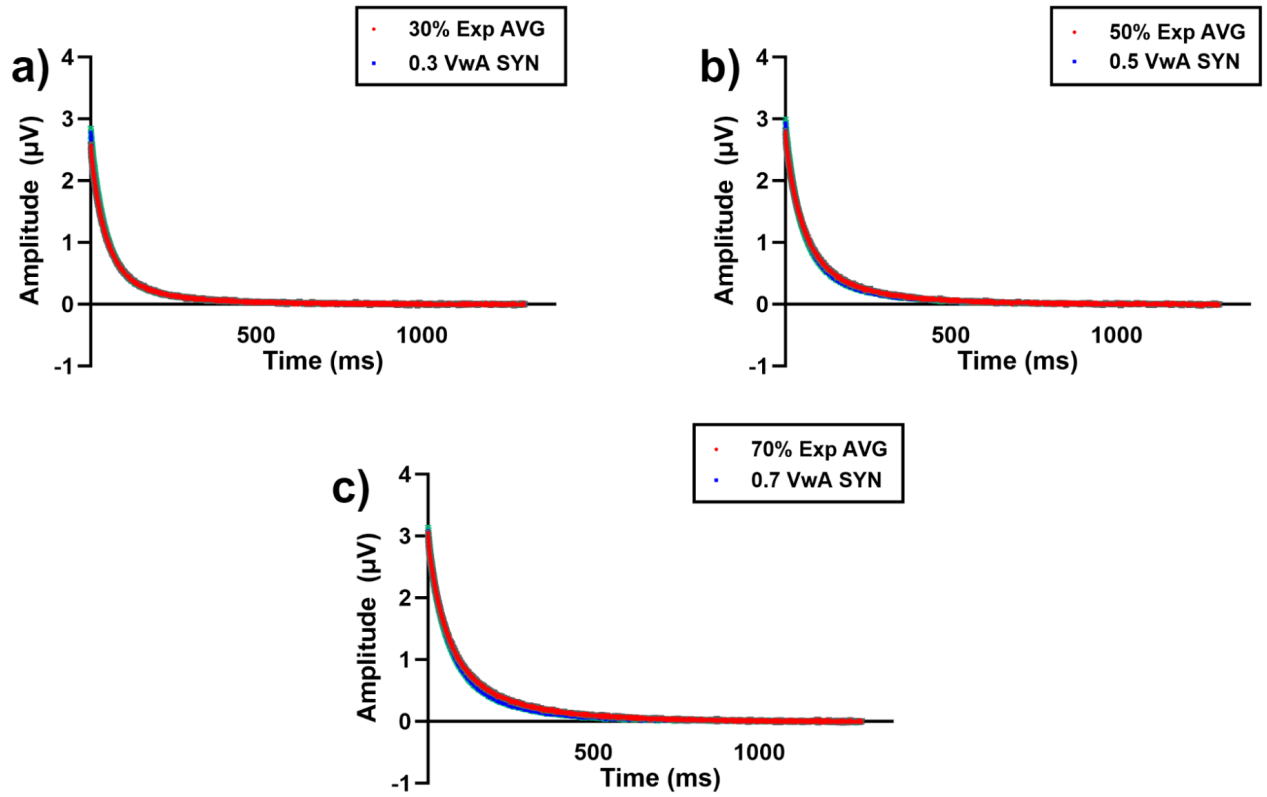

Figure 2-10. Comparison of Synthetic and Experimental T2 Relaxometry Data of a) 30% Oil Volume b) 50% Oil Volume and c) 70% Oil Volume Emulsions.

The experimental data in red consists of the average of five separate 10-minute data acquisitions in Figure 2-10 above. Each 10-minute acquisition was processed according to the established pipeline. The resulting five recommended averaged datasets for use were then averaged with each other. This is crucial due to the RF coil's extreme sensitivity to noise and other factors, all acquisitions for each emulsion were taken on the same day to minimize environmental variability. The error between the synthetic and experimental data increases as oil volume increases. This is most likely a reflection of the phenomenon of stimulated echoes in Figure 2-10. More pulses are applied but do not leave enough time for the protons to fully dephase,

additional pulses refocus some of the magnetization from the previous pulses, resulting in a stimulated echo during the pulse sequence. The amplitude and subsequent number of oil droplets dispersed in the same volume increases as the concentration of the oil phase increases. This phenomenon is more apparent when there are more oil droplets present although the stimulated echoes are occurring in each acquisition.

Figure 2-11 depicts the triexponential fit amplitudes of different oil volume fraction samples from data collected on the Li sensor. Figure 2-12 plots the subsequent relaxation times for each peak of the triexponential fit of the same data from Figure 2-11.

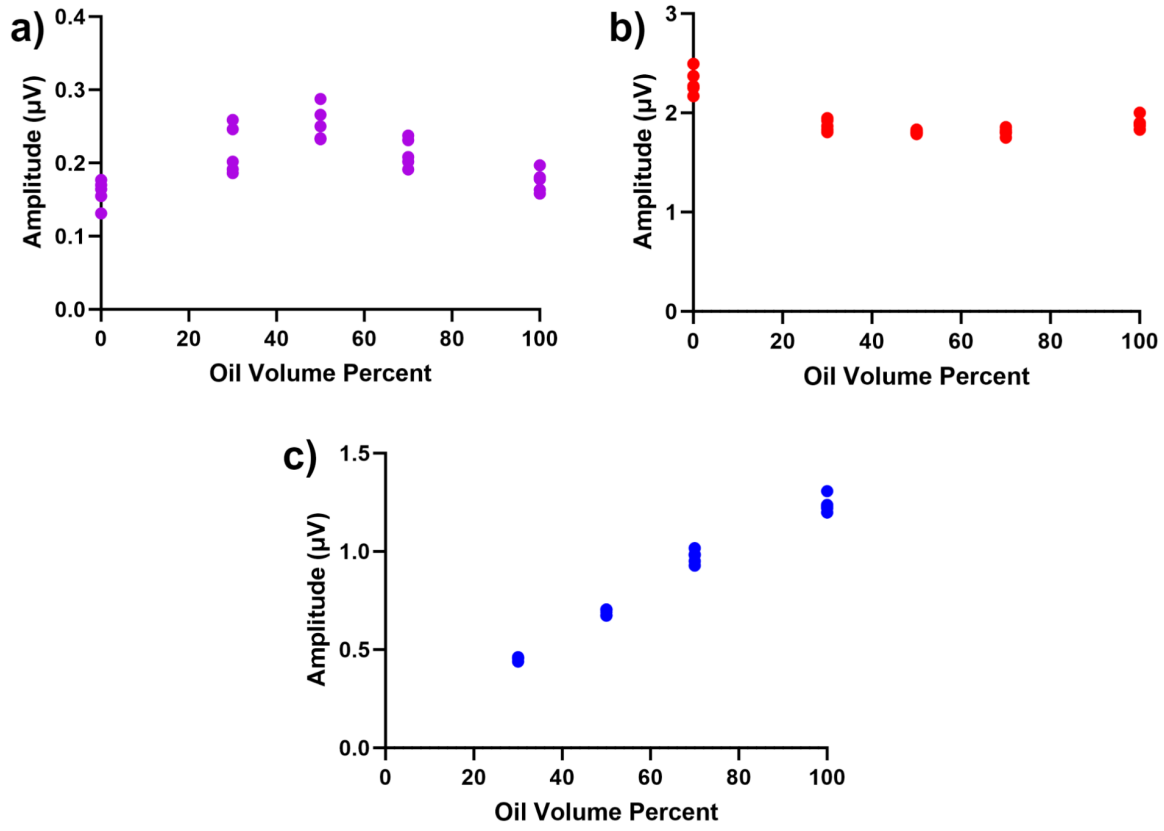

Figure 2-11. Amplitude components of a triexponential fit at varying oil volumes for a) peak 1, b) peak 2, and c) peak 3. Data collected on the Li sensor.

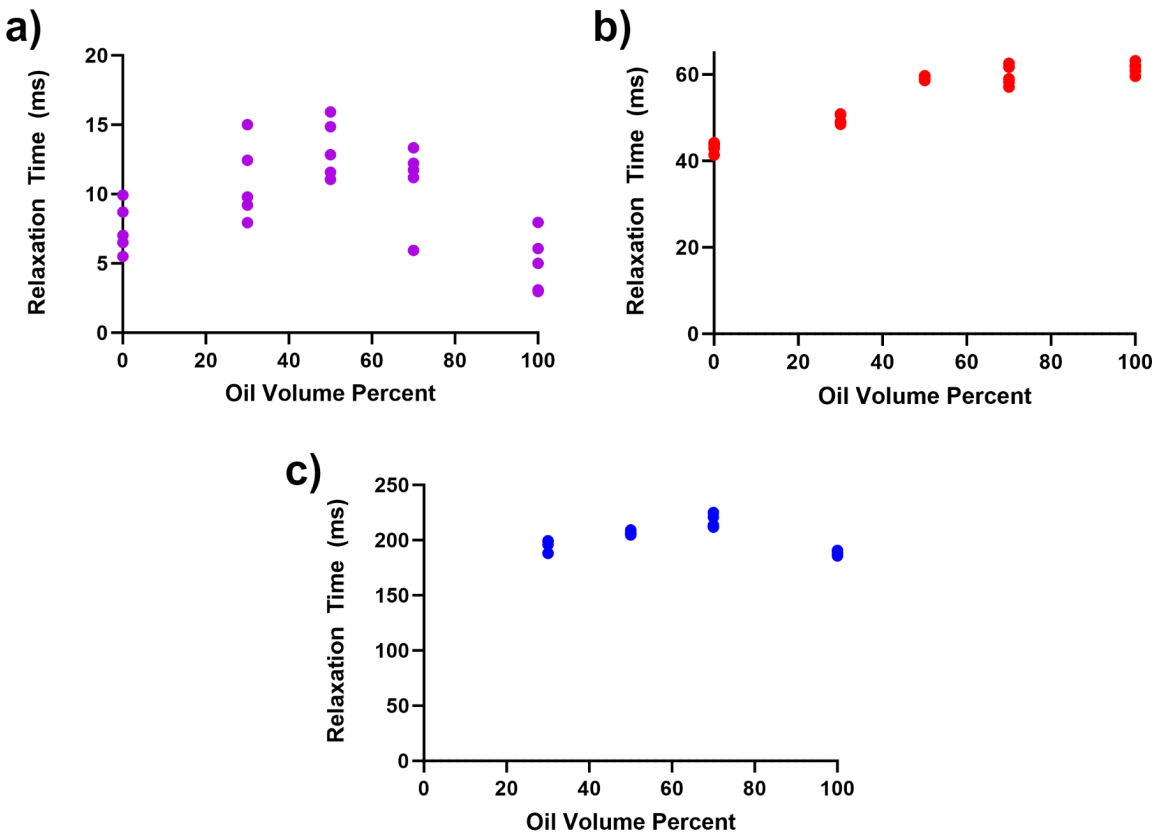

Figure 2-12. Relaxation time components of a triexponential fit at varying oil volumes for a) peak 1, b) peak 2, and c) peak 3. Data collected on the Li sensor.

A normalization factor is needed to compare amplitudes against each other because each sample has a different maximum amplitude for the y-intercept value. This normalization will enable analysis and comparison of each data point against the others by calculating relative amplitude. Relative amplitude compares the amplitude of a peak against the other measured amplitudes. Equation 2-6 contains an example for determining the relative amplitude of peak 3.

$$\%RA_3 = \frac{A_3}{(A_1+A_2+A_3)} * 100\% \quad (2\text{-}6)$$

The relative amplitude of each of the three peaks was calculated and plotted in Figure 2-13.

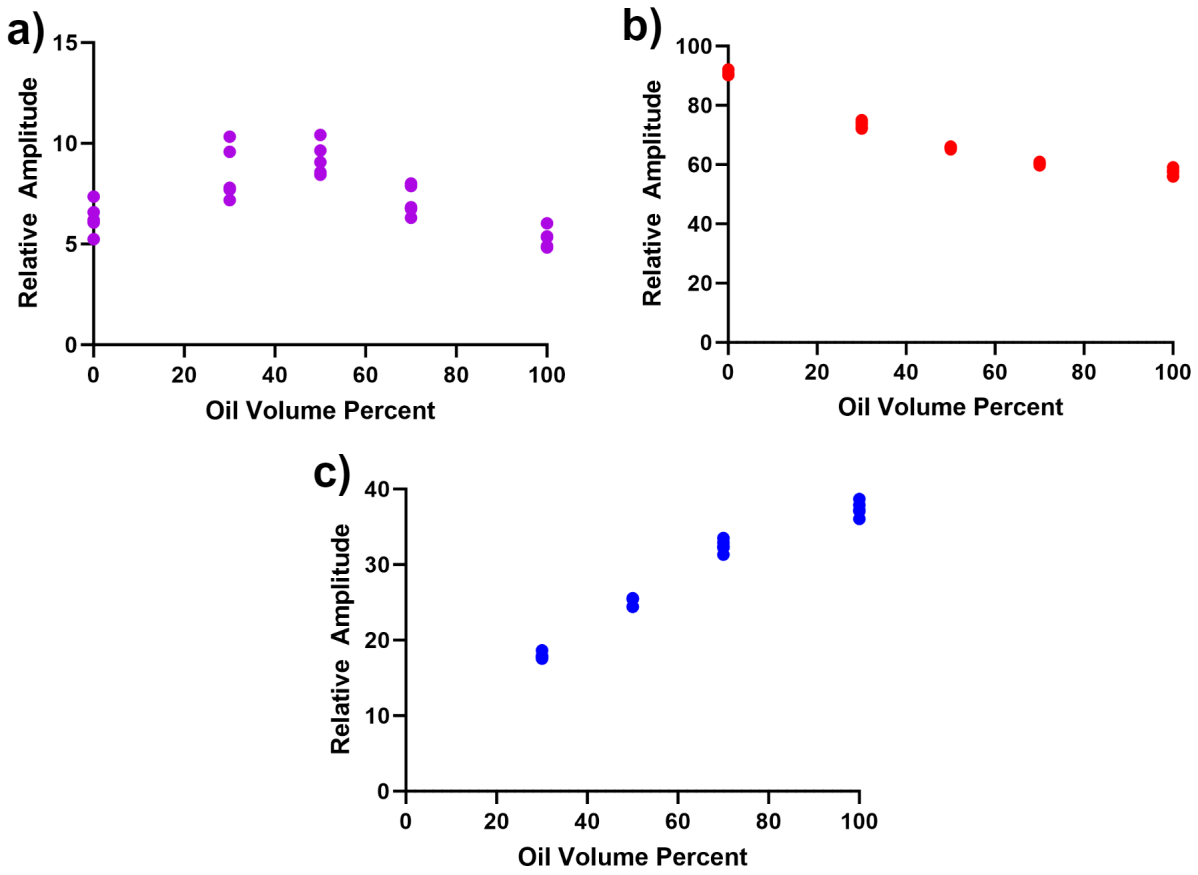

Figure 2-13. Relative amplitude components of a triexponential fit at varying oil volumes for a) peak 1, b) peak 2, and c) peak 3. Data collected on the Li sensor.

We expect to see the amplitude of peak 1 decrease since it should be representative of the aqueous phase. The amplitude of peaks 2 and 3 that are representative of the oil phase should increase with a higher volume fraction. Only the amplitude of the third peak shows an increase in amplitude with higher oil volumes. Figure 2-9 demonstrates that the raw relaxation of the emulsions behaves as a superposition of the volume-weighted averages of the aqueous and oil phases. The lack of agreement between this behavior and the triexponential fit results may stem from poor data processing and fitting. The triexponential fit contains six parameters and, according to Figure 2-10, should contain two peaks with relaxation times that are within 15 milliseconds of each other. It is likely that the code may fail to differentiate between the two

peaks that are close together in relaxation time. We will examine the components of the third peak for this reason.

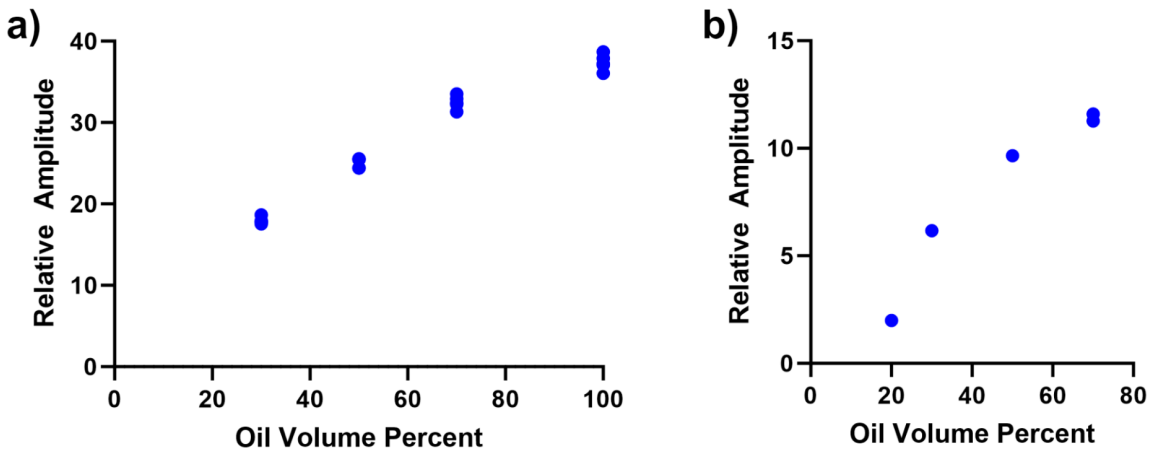

Figure 2-14. Relative amplitudes of peak 3 from a triexponential fit at varying oil volumes for data collected using a) the Li sensor and b) the Sherman sensor.

Figure 2-14 compares the relative amplitudes of peak 3 at different oil volume percentages, while Figure 2-15 compares the relaxation times fit to peak 3 for the same samples. The Sherman sensor exhibits the hypothesized behavior that the relaxation time does not change with oil volume, while the relative amplitude increases with oil volume. The relaxation behavior is not reflected in the fitted output from the Li sensor.

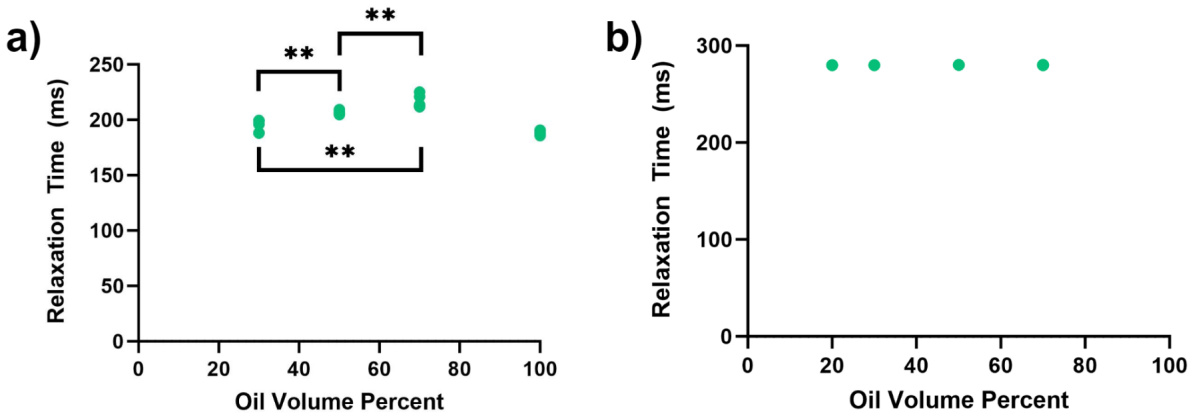

Figure 2-15. Relaxation times of peak 3 from a triexponential fit at varying oil volumes for data collected using a) the Li sensor and b) the Sherman sensor.

It is curious that the behavior of the two sensors exhibits such different results. The Sherman sensor shows that relaxation time does not change when oil volume increases while the Li sensor demonstrates an increase in relaxation time with increasing oil volume. One possible explanation for this is that the Sherman sensor only records the diffusion of protons within the oil droplets while the Li sensor is additionally recording diffusion between the oil droplets. This measurement of additional diffusion could explain the increasing relaxation time with increasing oil volume percent. The density of oil droplets increases throughout the emulsion and limits the diffusion and Brownian motion among the oil droplets as oil volume percent increases. More limited diffusion results in a longer relaxation time when diffusion between the oil droplets is recorded.

This explanation for the observed increasing relaxation time on the Li sensor makes sense except for the fact that it is only true for liquid emulsions. The emulsions are gels in the scintillation vials at the time of measurement. Coil temperature measurements were conducted to explore this.

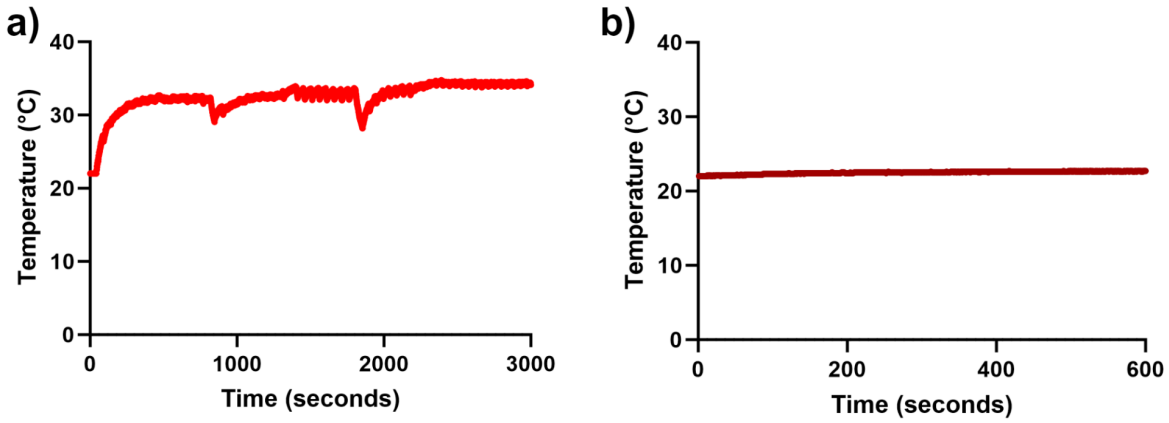

Figure 2-16. Coil temperatures of a) the Li sensor and b) the Sherman sensor when running CPMG pulse sequences.

An infrared thermometer (Testo, Pennsylvania, USA) was used to measure the temperature of the coil where a sample sits. CPMG pulse sequences were run similar to a typical data acquisition for both sensors. The two noticeable decreases in temperature in Figure 2-16a were from time increments where the CPMG pulse sequence was not running. The steady state operation temperature of the Li sensor is between 33°C and 34°C. Agar gels between 32 and 45°C. This means that agar can become unstable within this range. The temperature of the RF coil heating the emulsion combined with the instability of the agar can explain why the relaxation times for the Li sensor increase unexpectedly.

2.5: Microstructure Characterization

We sought to image the samples to gain a greater understanding of the microstructural characteristics of the emulsions. All imaging was conducted on the DeltaVision Ultra in the Koch Institute Microscopy Core Facility. The DeltaVision Ultra is an inverted confocal microscope with the ability to conduct both fluorescence and bright field microscopy on the

emulsions. Uniform sample thickness was important for sample imaging. This led us to use double-sided tape to create a box on the glass microscope slide. The double-sided tape boxes contained the emulsion samples and maintained an appropriate thickness. Z-stack images using both the Differential Interference Contrast (DIC) method of brightfield imaging and fluorescence imaging. These image stacks provide insight on the microstructure in three-dimensional space. Droplet size was measured by first selecting an image in the z-stack where the droplet diameter was maximized and in focus. This isolated image was loaded in ImageJ along with the metadata collected with the z-stack. This metadata includes the information regarding the calibration of pixels to a known distance. Isolated images were cropped down to a square of 512 by 512 pixels to minimize bias in droplet size measurements. The cropped section came from the direct center of every image. Every visible droplet diameter in the cropped image was measured. This was done to minimize biasing the measurements as much as possible.

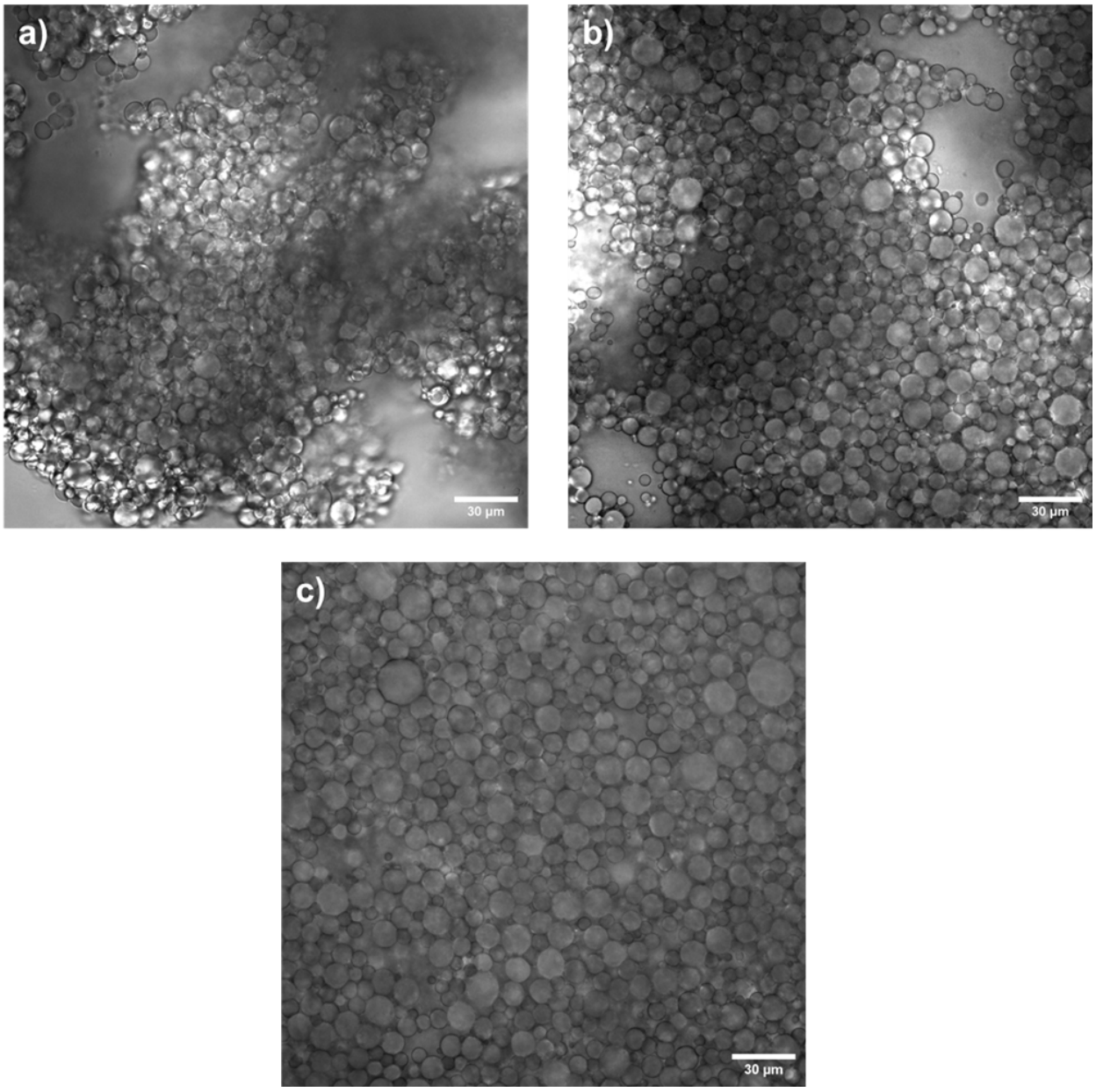

Figure 2-17. 40X Images of a) 20% oil volume emulsion, b) 50% oil volume emulsion, and c) 70% oil volume emulsion.

Figure 2-17 contains images of 20%, 50%, and 70% oil volume emulsions that were created in accordance with the methods outlined in Section 2.2. Figure 2-18 shows the cropped and measured images for the samples shown in Figure 2-17. The average measured droplet diameter and standard deviation for each sample are listed in Table 2-1.

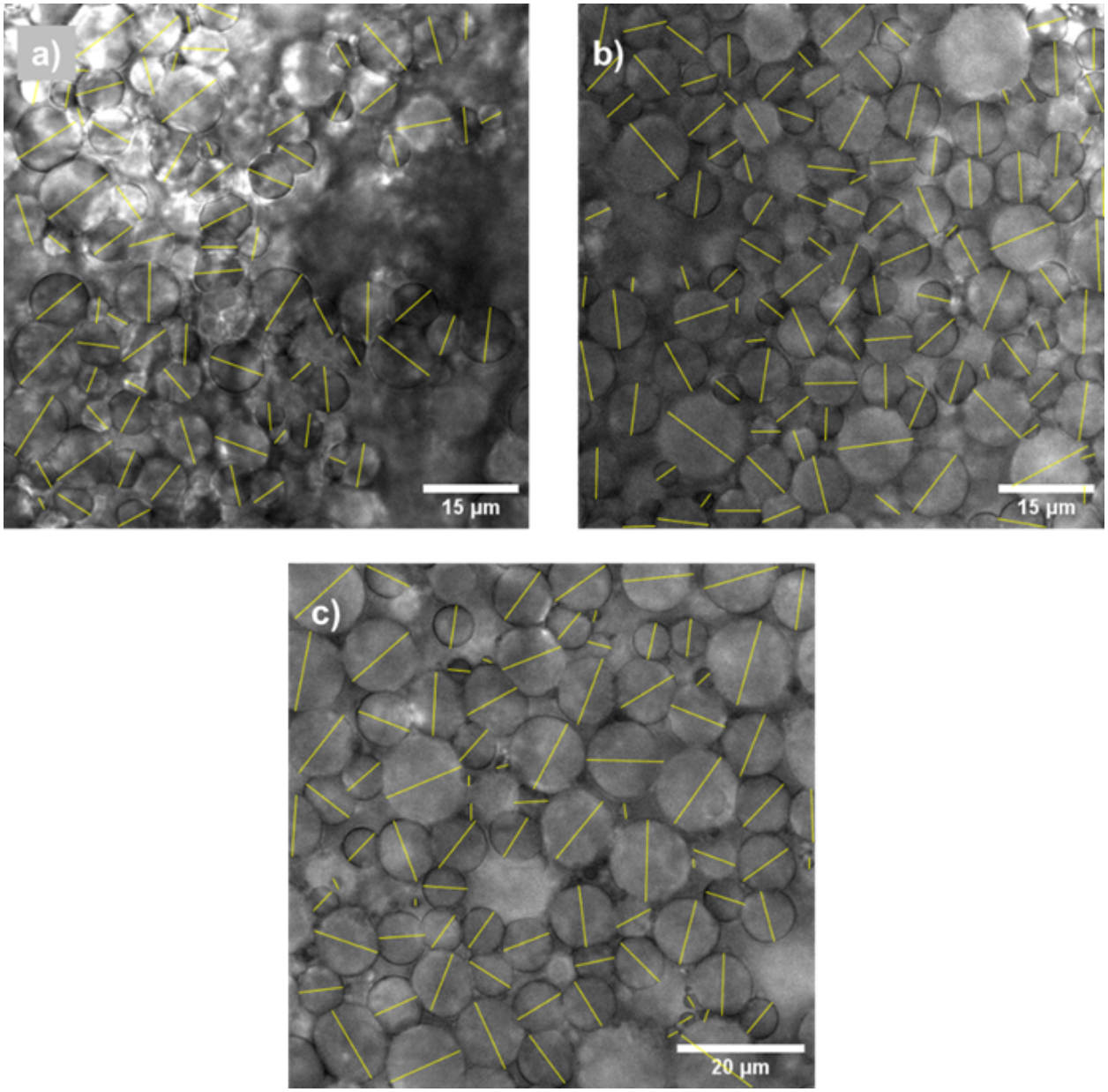

Figure 2-18. Cropped and measured images of a) 20% oil volume emulsion, b) 50% oil volume emulsion, and c) 70% oil volume emulsion.

It is important to remember that there are other valuable metrics that can be used to characterize microstructure in addition to measured droplet diameter. Different emulsions contain varying oil volumes in addition to the fact that the oil droplets are three dimensional. One way to ensure that these factors are accounted for in characterizing the microstructure of the emulsions is to

calculate a volume-weighted average of the droplet diameters, D_{vw}. This value can be calculated using equation 2-7 where D_i is the measured droplet diameter and V_i is the calculated volume of the droplet. This metric is also recorded in Table 2-1.

$$D_{vw} = \frac{\sum_{i=1}^{n} (D_i * V_i)}{\sum_{i=1}^{n} V_i} \tag{2-7}$$

Oil Volume	Average Diameter (µm)	Standard Deviation (µm)	Volume-Weighted Average Diameter (µm)
20%	6.55	2.41	8.74
50%	6.52	2.51	8.88
70%	7.59	3.49	10.54

Table 2-1. Average and volume-weighted diameters and corresponding standard deviation for droplet size measurements.

2.6: Relaxation Properties and Microstructure Variation

Our research investigated the potential impact of droplet size on T2 relaxation time in emulsions. Changes in microstructure were made to explore the variation of microstructure characteristics as a result of emulsion formation. We employed varying mixing rates and durations as a means to mechanically alter the sizes of the dispersed oil droplets. These droplets were measured from images captured on the DeltaVision Ultra microscope.

We regulated the mixing rate to a range between 100 and 200 revolutions per minute (rpm) during the oil addition process to obtain larger oil droplets. This approach, however, presented

certain challenges. Achieving emulsification and maintaining the stability of the emulsion proved to be a complex task. This resulted in an extended amount of mixing time required for the creation of the emulsions. The emulsions were mixed at this controlled rate for an additional five minutes to ensure uniformity after the oil fully incorporated.

The formation of smaller droplets necessitated a significantly higher stirring rate, ranging between 1450 and 1600 rpm. It is important to note that 1600 rpm represents the maximum operational stir rate of our laboratory hot plate. This high-speed stirring, however, occasionally led to the stir bar being ejected from its position, causing it to bounce erratically within the flask. Such instances necessitated an immediate reduction in the stirring rate to prevent the stir bar from being thrown out. This adjustment was crucial for maintaining continuous and effective mixing, thereby ensuring the consistent formation of smaller droplets.

Figure 2-19 depicts the visual difference in droplet size where all images were taken at the same magnification. Table 2-2 shows the characteristics of each microstructure developed at each shear rate.

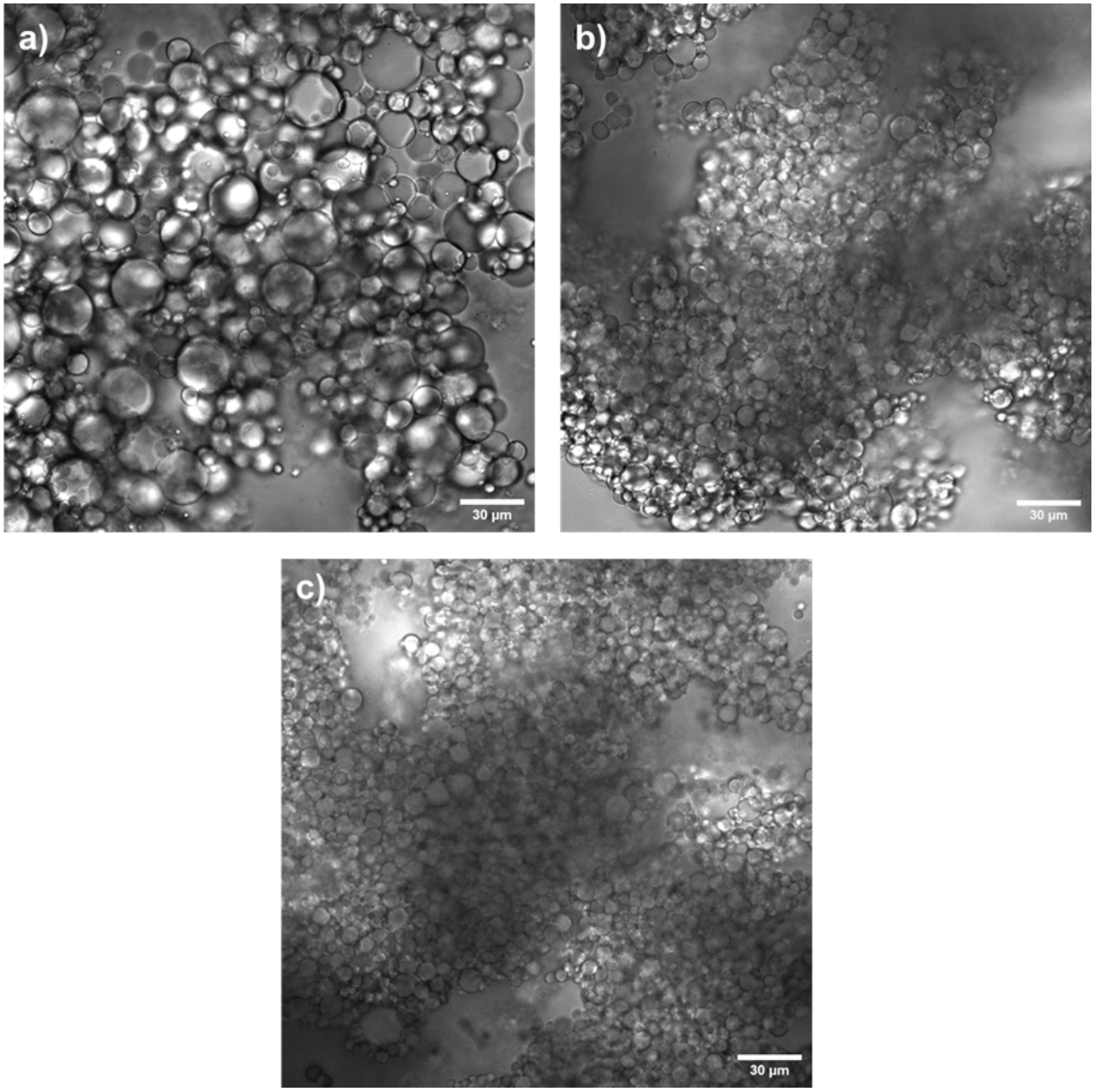

Figure 2-19. 20% Oil volume emulsions created under a) low shear conditions, b) original method, and c) high shear conditions.

20% Oil Volume Shear Rate	Average Diameter (µm)	Standard Deviation (µm)	Volume-Weighted Average Diameter (µm)
Low Shear	9.86	7.76	22.46
Original Method	6.55	2.41	8.74
High Shear	4.00	1.56	5.78

Table 2-2. 20% Oil volume emulsions characteristics with different creation conditions.

Similarly the same shear rates and microstructure analysis were conducted for 50% oil volume emulsions as shown in Figure 2-20 and Table 2-3 below.

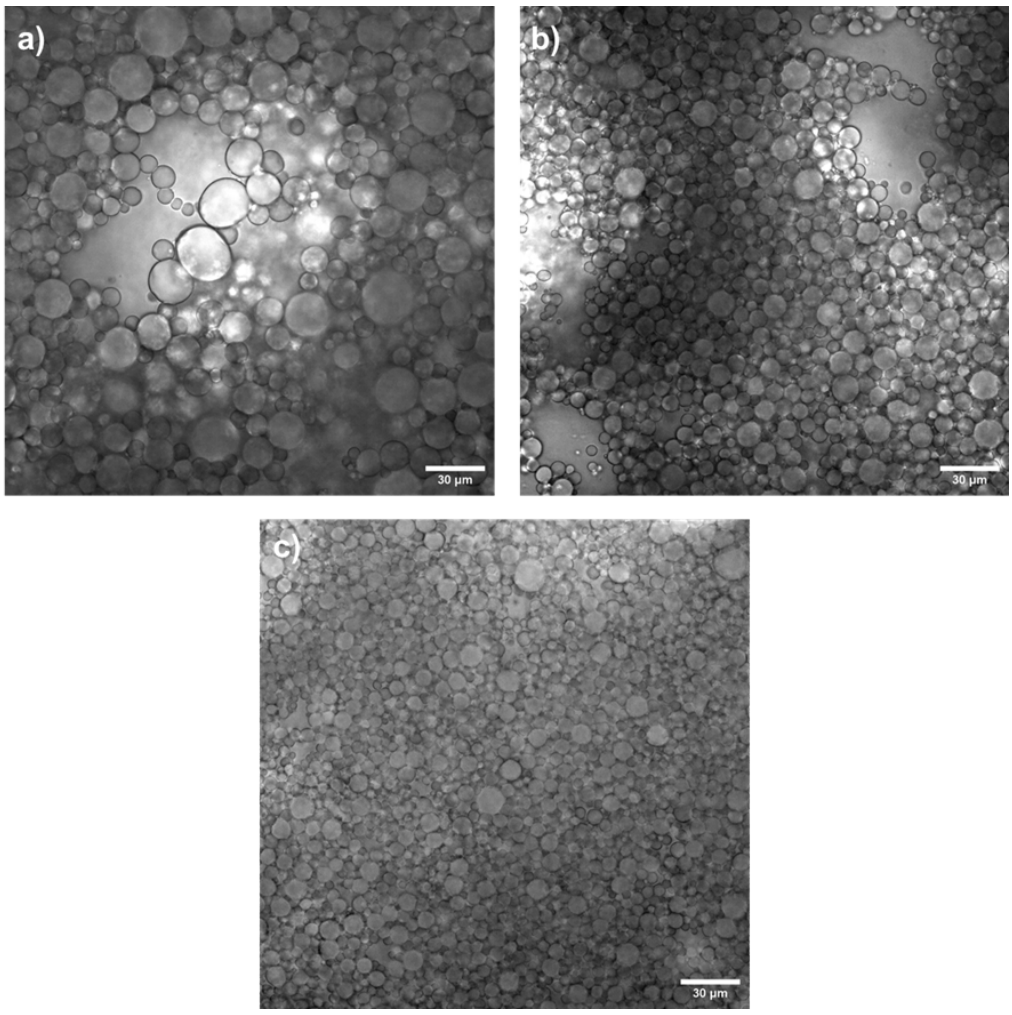

Figure 2-20. 50% Oil volume emulsions created under a) low shear conditions, b) original method, and c) high shear conditions.

50% Oil Volume Shear Rate	Average Diameter (µm)	Standard Deviation (µm)	Volume-Weighted Average Diameter (µm)
Low Shear	12.41	5.31	18.21
Original Method	6.52	2.51	8.88
High Shear	5.16	1.96	7.12

Table 2-3. 50% Oil volume emulsions characteristics with different creation conditions.

The relaxation data was collected on these samples to determine if these differences in microstructure were reflected in the relaxation behavior of the samples. The relaxation time of peak 3 is explored in particular. This is because relaxation time is most likely to be impacted by droplet size. This is because proton diffusion within a droplet may change with droplet size and needs to be examined. Figure 2-15a shows that there is statistical significance between the relaxation times as a function of oil volume percentage. This means that relaxation time and droplet diameter can only be compared when every data point has the same oil volume percentage.

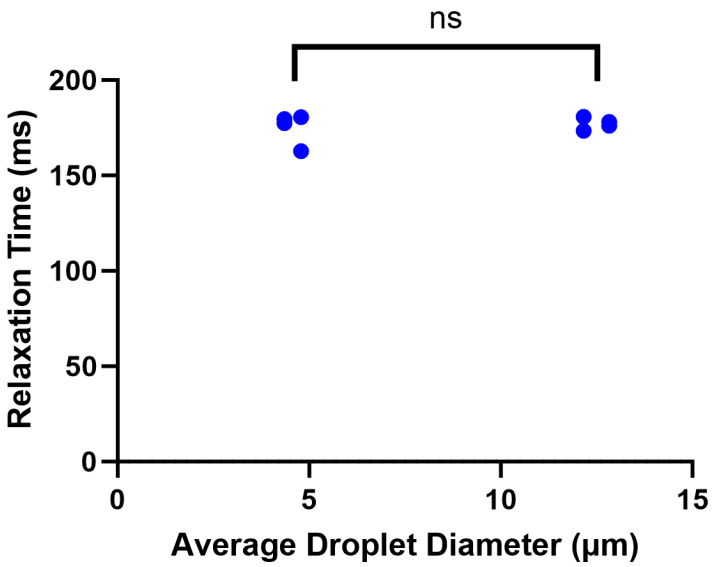

Figure 2-21. Droplet relaxation time of a 20% oil volume sample as droplet diameter increases.

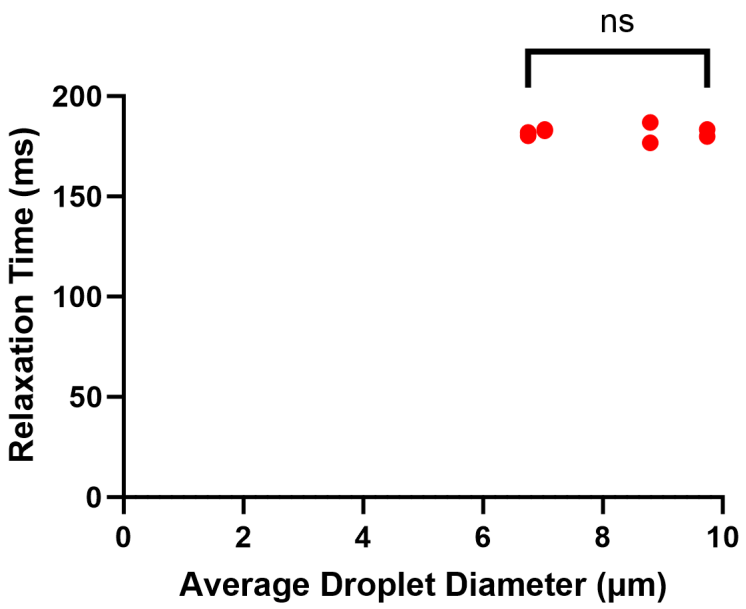

Figure 2-22. Droplet relaxation time of a 50% oil volume sample as droplet diameter increases.

Both Figures 2-21 and 2-22 do not contain statistically significant differences between the relationships between the relaxation times and changes in droplet size for a given oil volume percentage. This means that the relaxation properties of the emulsions are resistant to variation in the microstructure.

Chapter 3

Theoretical Assessment of Emulsions

3.1: Background

Two immiscible components, such as oil and water, can form emulsions under certain conditions. In an emulsion, one component is suspended as the dispersed phase within the continuous phase of the other component. The components of the dispersed and continuous phases impact the properties and potential uses of the emulsions. For example, butter and sunscreen are water in oil emulsions used every day. Oil in water emulsions also exist in everyday consumer products such as moisturizers, homogenized milk, and mayonnaise[40]

Phantoms are cost-effective, minimize animal testing, and can maintain quality assurance in both preclinical and clinical validation of Cima lab's MR device[31]. A deeper understanding of the properties of the emulsions is needed in order to have confidence in using the emulsions as phantoms for the NMR device. Here, the behavior of the emulsions as colloids are explored to analyze the theoretical stability of the emulsions. Furthermore, the behavior of the interaction between emulsions and glass surfaces are studied. This will provide further insight to whether the properties and stability of the emulsion are impacted by containers such as microscope slides and scintillation vials.

3.2: Modeling Stability and Emulsification Conditions

The mixing conditions additionally have a significant effect on the overall stability of emulsions. This is because the interfacial characteristics of the oil, water, and emulsifying agents are dependent on thermodynamic conditions[40]. Such factors including temperature, mixing rate, and oil volume percentage are shown to change the physical properties of the droplets in the dispersed phase. It is important to note that when considering the oil volume percentage of an oil in water emulsion, it should not exceed 74%, as the emulsion may become more densely packed than possible which may result in phase inversion or breaking[41]. Temperature impacts emulsification through the change in interfacial tension, adsorption, and viscosity[40], [41]. Generally, an increase in temperature will result in more favorable conditions for emulsification; however, an abrupt change in temperature can cause coagulation in the emulsions, which result in lower stability[41]. Both the surface tension and viscosity decrease with increasing temperature. The subsequent increased kinetic energy imparted to the surface molecules at higher temperature will tend to overcome the net attractive force of the bulk liquid (water)[41]. This is demonstrated in Eotvos's Equation[42]:

$$\gamma(Mv)^{2/3} = \kappa(T_C - T) \tag{3-1}$$

γ is the surface free energy, M is the molecular weight, v is the specific volume, T_C is the critical temperature of the liquid, T is the temperature, and κ is a universal constant (which is approximately 2.2 for many liquids). As temperature increases and approaches the critical temperature of the liquid, the surface free energy decreases, indicating a higher likelihood of achieving emulsification.

Emulsification is typically achieved through the application of mechanical energy. Stirring is critical to ensure that the large droplets of the dispersed phase are broken up into

smaller droplets, which is a function of stir rate and stir intensity[41]. Additionally, mixing time is important as increasing mixing time is effective for making emulsions until intense stirring may cause the emulsifier to drop out from the oil-water interface, preventing further emulsification. This results in an optimal mixing time that depends on the surfactants and mixing rate used[41], [43]. The stability of an emulsion can be generalized and determined through a force balance can be used to determine settling rate of emulsions using Stoke's Law[40]:

$$V_{STOKES} = \frac{(\rho_d - \rho_c) g d^2}{18\mu_c} \tag{3-2}$$

V_{STOKES} is the sedimentation velocity, ρ_d and ρ_c are the densities of the dispersed and continuous phases, g is the acceleration due to gravity, d is the corresponding droplet diameter, and μ_c is the dynamic viscosity of the continuous phase in Equation 3-2. One limitation to Equation 3-2 is that it does not account for particles that are not spherical and the interaction between particles. The Hadamard-Rybczynski equation can be used when correcting for this[40]:

$$V_{HR} = \frac{(\rho_d - \rho_c) g d^2}{18\mu_c} \frac{\mu_c + \mu_d}{\frac{2}{3}\mu_c + \mu_d} \tag{3-3}$$

where V_{HR} includes a correction term for viscosity and μ_d is the viscosity of the dispersed phase.

Conventional emulsions are inherently thermodynamically unstable systems because over time, the interfacial energy will decrease and dispersed droplets will coalesce and phase separate[44]. This is why tween 20 and span 80 are used for further stability in the emulsions. Generally, a single surfactant cannot produce the desired stability in an emulsion[43]. Both tween 20 and span 80 were chosen for the nonionic properties and tendency for stabilizing oil in water emulsions for the purpose of mimicking muscle and adipose tissue.

Tween 20 is a nonionic hydrophilic surfactant. It is a polyoxyethylene sorbitol ester that consists of 20 ethylene oxide units, 1 sorbitol, and 1 lauric acid. The ethylene oxide subunits are responsible for the hydrophilic nature of the surfactant, while the hydrocarbon chains provide a hydrophobic environment (Millipore Sigma). Span 80 is a nonionic surfactant. It is a sorbitan carboxyl ester that is hydrophobic (Millipore Sigma). Surfactants contain surface tension and interfacial tension properties that impact the interface between components in the emulsion. Subsequently, the adsorption capabilities of the surfactants are also connected to the wetting properties[45]. Both the hydrophobic and hydrophilic nature of the surfactants interact with the oil and water components of the emulsion in this way. This stabilizes the emulsion by regulating the interfacial tension across the interface. One potential change that may make the emulsion more stable is to use span 20 instead of span 80. This is because when analyzing the properties of different kinds of surfactants, one variable, the hydrophile-lypophile balance (HLB) for characterizing surfactants was clear. Surfactants with a higher HLB value are better suited for oil-in-water emulsions whereas surfactants with a lower HLB value are better suited for water-in-oil emulsions[44]. Span 80 has an HLB value of 4.3, whereas span 20 has an HLB value of 8.6[46]. Since the difference between span 80 and span 20 reasonable, it may be beneficial to experiment with using span 20 instead of span 80 in future work using oil-in-water emulsions.

The agar component of the emulsions is added to stabilize and prevent phase separation through coalescence, flocculation, creaming, sedimentation, or Ostwald ripening. Many emulsions, to include food emulsions, contain texture modifiers that either increase the viscosity of the continuous phase as a thickening agent, or form a gel network within the continuous phase. This enables the motion of the dispersed droplets to be slowed down either due to gravity or Brownian motion[47]. Common gelling or thickening agents include agar, cellulose, starch,

alginate, soy and egg protein[47]. The creaming stability and extent of droplet aggregation can be modeled with an interaction potential w(h), the energy required to bring two emulsion droplets from an infinite distance apart to a surface-to-surface separation of h:

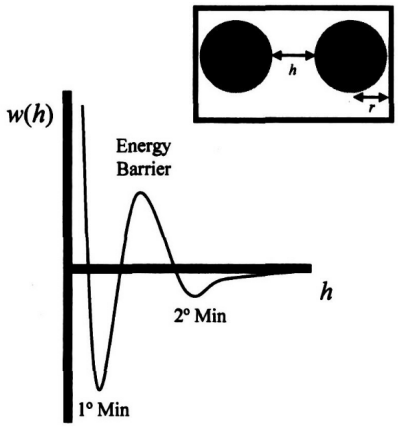

Figure 3-1. Schematic representation of the interaction potential between two emulsion droplets showing the primary minimum (1° Min), secondary minimum (2° Min) and energy barrier[47].

Agar only mixes with the water component. The peanut oil component is not part of the gel matrix and likely experiences distortion as a result of compression[48]. This can be modeled by:

$$S = 2\pi\left(a^2 + \frac{c^2}{2e}\log log\left(\frac{1+e}{1-e}\right)\right) \tag{3-4}$$

S is the surface area of the ellipsoid where the volume, $V = \pi a^2 c\frac{4}{3}$ is constant, and e is eccentricity. a and c are the major and minor axes, and when $a > c$, $e = 1 - \frac{c^2}{a^2}$. This model postures that the difference in gel strength across different emulsions is a function of varying diameter oil droplets that is likely a result of the difference in distortion resistance within the gels[48]. While the agar largely provides stability to the overall emulsion, it also maintains uniformity with the oil droplets even with some potential distortion[49].

An examination into the ionic and non-ionic components of the emulsion is necessary because the stability of the emulsions depends on the forces between the components. The main sources of force largely originate from van der Waals forces, electrostatic forces, or solvent forces[50]. Van der Waals forces exist between all particles; the magnitude between two bodies, such as the dispersed and continuous phases, can be quantified by the Hamaker constant. The Hamaker constant is larger when the interaction between the two bodies is larger. It can be modeled using the equation:

$$A_H = \pi^2 * C_{AB} * \rho_A * \rho_B \tag{3-6}$$

ρ_A and ρ_B are the densities of the interacting phases and C_{AB} is the London coefficient where:

$$C_{AB} = \frac{3}{4} * \frac{\alpha_A \alpha_B I_A I_B}{(I_A + I_B)} \tag{3-7}$$

α_A and α_B are the polarizability of each component, and I_A and I_B are the ionization energies of the components.

3.3: Bi-Droplet Collisions

The collision kinetics of droplets in an emulsion are governed by factors such as relative velocity, droplet size, and the viscosity of the continuous phase. Collision outcomes consist of coalescence, stretching separation, or bouncing. These outcomes are determined by the balance of kinetic energy and surface energy during the impact. Studies have shown that with increasing droplet viscosity, the boundary for the coalescence and stretching separation transition shifts[51]. This indicates that internal droplet fluid dynamics strongly impact the outcome of bi-droplet collisions[52]. Temperature and surfactant presence are external factors that can impact collision

outputs by altering the interfacial tension of the droplets and, subsequently, the collision behavior[53].

Surface interactions in bi-droplet collisions largely involve interfacial characteristics such as surface tension and surfactant dynamics. The continuous phase between two droplets leaves as they approach each other and the film between the two droplets drains. The film between the droplet ruptures and results in coalescence when the film reaches a critical thickness. The dynamics of the continuous phase leaving is influenced by both the properties of the droplets and the continuous phase. The adsorption-desorption kinetics combined with a surfactant's ability to reduce surface tension play an important role in collision outcomes of emulsions stabilized by surfactants. Surfactants can either promote or inhibit coalescence depending on the properties and concentration. High surfactant concentrations can form rigid interfacial films that prevent droplet coalescence and result in more stable emulsions.

Temperature can significantly influence the kinetics and surface interactions of bi-droplet collisions. Temperature changes impact the viscosity of the droplets and the continuous phase as well as the surface tension at the interface between the dispersed phase and continuous phase. Increasing temperature typically increases the coalescence rate due to decreased viscosity and surface tension[53], [54].

The kinetics and surface interactions of bi-droplet collisions within emulsions are complex and impacted by many factors. Understanding the behavior of these interactions enables us to better understand our emulsions in complex systems; such as for use as human muscle tissue phantoms on an MR device.

Chapter 4

Conclusion

We developed synthetic T2 relaxation data by combining the characteristics of aqueous and oil components using a volume-weighted average based on the volume of the oil component in this study. This approach effectively produced a synthetic dataset that closely aligned with the experimental data we collected. This alignment confirms our hypothesis that the relaxation behavior of emulsions is indeed a superposition of their individual components' characteristics.

Discrepancies regarding confirming our superposition hypothesis emerged when analyzing fit results at the faster relaxation times of peaks 1 and 2. The results were obtained using a triexponential fit where the discrepancies likely originated from the inherent limitations of our fitting approach. The triexponential fit solves for six parameters and does not have many boundary conditions to avoid making incorrect assumptions. This observation highlights the need for a more nuanced model or fitting strategy to accurately capture the dynamics of the system.

Further insights into the emulsions' microstructure were gained through optical microscopy and image analysis. We effectively manipulated microstructure characteristics such as oil droplet size and distribution by varying the mixing rate and duration. It is notable that despite these variations in microstructure, emulsions with identical oil volume fractions exhibited similar relaxation behavior. This finding is significant for the application of these emulsions as phantoms for use

with MR devices, suggesting a level of reliability and predictability in their performance, regardless of minor variations in emulsion preparation methods.

A priority for future work in this area should be the development of more sophisticated data processing techniques. Such advancements would enhance the reliability and accuracy of the fits, thereby providing more precise and meaningful insights into the relaxation behaviors of these complex emulsions. This progression will not only refine our understanding of the fundamental properties of emulsions but also bolster their application in various scientific and industrial contexts.

Bibliography

[1] B. M. Popkin, K. E. D'Anci, and I. H. Rosenberg, "Water, hydration, and health: Nutrition Reviews©, Vol. 68, No. 8," *Nutr. Rev.*, vol. 68, no. 8, pp. 439–458, Aug. 2010, doi: 10.1111/j.1753-4887.2010.00304.x.

[2] K. Kalantar-Zadeh *et al.*, "Fluid retention is associated with cardiovascular mortality in patients undergoing long-term hemodialysis," *Circulation*, vol. 119, no. 5, pp. 671–679, Feb. 2009, doi: 10.1161/CIRCULATIONAHA.108.807362.

[3] E. Chaney and A. Shaw, "Pathophysiology of Fluid Retention in Heart Failure," May 2010, doi: 10.1159/000313720.

[4] D. R. Thomas *et al.*, "Understanding Clinical Dehydration and Its Treatment," *J. Am. Med. Dir. Assoc.*, vol. 9, no. 5, pp. 292–301, Jun. 2008, doi: 10.1016/j.jamda.2008.03.006.

[5] R. Maulana, D. Syauqy, and R. Z. Amani, "Dehydration Level Detection System Based on Urine Condition," in *Proceedings of the 9th International Conference on Signal Processing Systems*, in ICSPS 2017. New York, NY, USA: Association for Computing Machinery, Nov. 2017, pp. 207–210. doi: 10.1145/3163080.3163118.

[6] N. Reljin *et al.*, "Automatic Detection of Dehydration using Support Vector Machines," in *2018 14th Symposium on Neural Networks and Applications (NEUREL)*, Nov. 2018, pp. 1–6. doi: 10.1109/NEUREL.2018.8587008.

[7] S. Alsanie, S. Lim, and S. A. Wootton, "Detecting low-intake dehydration using bioelectrical impedance analysis in older adults in acute care settings: a systematic review," *BMC Geriatr.*, vol. 22, no. 1, p. 954, Dec. 2022, doi: 10.1186/s12877-022-03589-0.

[8] H. C. Lukaski, N. Vega Diaz, A. Talluri, and L. Nescolarde, "Classification of Hydration in Clinical Conditions: Indirect and Direct Approaches Using Bioimpedance," *Nutrients*, vol. 11, no. 4, p. 809, Apr. 2019, doi: 10.3390/nu11040809.

[9] L. E. Armstrong, "Assessing Hydration Status: The Elusive Gold Standard," *J. Am. Coll. Nutr.*, vol. 26, no. sup5, pp. 575S-584S, Oct. 2007, doi: 10.1080/07315724.2007.10719661.

[10] O. R. Barley, D. W. Chapman, and C. R. Abbiss, "Reviewing the current methods of assessing hydration in athletes," *J. Int. Soc. Sports Nutr.*, vol. 17, no. 1, p. 52, Oct. 2020, doi: 10.1186/s12970-020-00381-6.

[11] I. S. Edelman and J. Leibman, "Anatomy of body water and electrolytes," *Am. J. Med.*, vol. 27, no. 2, pp. 256–277, Aug. 1959, doi: 10.1016/0002-9343(59)90346-8.

[12] I. Lorenzo, M. Serra-Prat, and J. C. Yébenes, "The Role of Water Homeostasis in Muscle Function and Frailty: A Review," *Nutrients*, vol. 11, no. 8, Art. no. 8, Aug. 2019, doi: 10.3390/nu11081857.

[13] A. Segal, "Disorders of Extracellular Volume: Hypovolemia and Hypervolemia," in *CURRENT Diagnosis & Treatment: Nephrology & Hypertension*, 2nd ed., E. V. Lerma, M. H. Rosner, and M. A. Perazella, Eds., New York, NY: McGraw-Hill Education, 2017.

Accessed: Jan. 13, 2024. [Online]. Available: accessmedicine.mhmedical.com/content.aspx?aid=1149111418

[14] L. E. Armstrong, J. A. H. Soto, F. T. Hacker, D. J. Casa, S. A. Kavouras, and C. M. Maresh, "Urinary Indices during Dehydration, Exercise, and Rehydration," *Int. J. Sport Nutr. Exerc. Metab.*, vol. 8, no. 4, pp. 345–355, Dec. 1998, doi: 10.1123/ijsn.8.4.345.

[15] L. A. Popowski, R. A. Oppliger, G. Patrick Lambert, R. F. Johnson, A. Kim Johnson, and C. V. Gisolfi, "Blood and urinary measures of hydration status during progressive acute dehydration," *Med. Sci. Sports Exerc.*, vol. 33, no. 5, p. 747, May 2001.

[16] S. F. Khalil, M. S. Mohktar, and F. Ibrahim, "The Theory and Fundamentals of Bioimpedance Analysis in Clinical Status Monitoring and Diagnosis of Diseases," *Sensors*, vol. 14, no. 6, pp. 10895–10928, Jun. 2014, doi: 10.3390/s140610895.

[17] A. Piccoli, "Whole Body – Single Frequency Bioimpedance," May 2005, doi: 10.1159/000085478.

[18] P. Kotanko, N. W. Levin, and F. Zhu, "Current state of bioimpedance technologies in dialysis," *Nephrol. Dial. Transplant.*, vol. 23, no. 3, pp. 808–812, Mar. 2008, doi: 10.1093/ndt/gfm889.

[19] V. Leonov, S. Lee, A. Londergan, R. A. Martin, W. De Raedt, and C. Van Hoof, "Bioimpedance Method for Human Body Hydration Assessment," in *2019 41st Annual International Conference of the IEEE Engineering in Medicine and Biology Society (EMBC)*, Jul. 2019, pp. 6036–6039. doi: 10.1109/EMBC.2019.8857207.

[20] K. Cumming, G. E. Hoyle, J. D. Hutchison, and R. L. Soiza, "Bioelectrical impedance analysis is more accurate than clinical examination in determining the volaemic status of elderly patients with fragility fracture and hyponatraemia," *J. Nutr. Health Aging*, vol. 18, no. 8, pp. 744–750, 2014, doi: 10.1007/s12603-014-0539-8.

[21] J. Lacey *et al.*, "A multidisciplinary consensus on dehydration: definitions, diagnostic methods and clinical implications," *Ann. Med.*, vol. 51, no. 3–4, pp. 232–251, doi: 10.1080/07853890.2019.1628352.

[22] W. L. Kenney and P. Chiu, "Influence of age on thirst and fluid intake," *Med. Sci. Sports Exerc.*, vol. 33, no. 9, pp. 1524–1532, Sep. 2001, doi: 10.1097/00005768-200109000-00016.

[23] D. L. Duren *et al.*, "Body Composition Methods: Comparisons and Interpretation," *J. Diabetes Sci. Technol.*, vol. 2, no. 6, pp. 1139–1146, Nov. 2008, doi: 10.1177/193229680800200623.

[24] A. Bashyam *et al.*, "A portable single-sided magnetic-resonance sensor for the grading of liver steatosis and fibrosis," *Nat. Biomed. Eng.*, vol. 5, no. 3, pp. 240–251, Nov. 2020, doi: 10.1038/s41551-020-00638-0.

[25] L. A. Colucci *et al.*, "Fluid assessment in dialysis patients by point-of-care magnetic relaxometry," *Sci. Transl. Med.*, vol. 11, no. 502, p. eaau1749, Jul. 2019, doi: 10.1126/scitranslmed.aau1749.

[26] A. Bashyam, M. Li, and M. J. Cima, "Design and experimental validation of Unilateral Linear Halbach magnet arrays for single-sided magnetic resonance," *J. Magn. Reson.*, vol.

292, pp. 36–43, Jul. 2018, doi: 10.1016/j.jmr.2018.05.004.

[27] S. E. Sherman, A. S. Zammit, W.-S. Heo, M. S. Rosen, and M. J. Cima, “Single-sided magnetic resonance-based sensor for point-of-care evaluation of muscle,” *Nat. Commun.*, vol. 15, no. 1, Art. no. 1, Jan. 2024, doi: 10.1038/s41467-023-44561-9.

[28] “What Are Imaging Phantoms?,” *NIST*, Apr. 2018, Accessed: Dec. 30, 2023. [Online]. Available: https://www.nist.gov/physics/what-are-imaging-phantoms

[29] E. Bush C., A. Gifford, C. L. Coolbaugh, T. F. Towse, B. M. Damon, and E. B. Welch, “Fat-Water Phantoms for Magnetic Resonance Imaging Validation: A Flexible and Scalable Protocol.” Accessed: Dec. 04, 2023. [Online]. Available: https://app.jove.com/t/57704/fat-water-phantoms-for-magnetic-resonance-imaging-validation-a-flexible-and-scalable-protocol

[30] G. Gambarota, R. L. Janiczek, R. V. Mulkern, and R. D. Newbould, “An NMR Phantom Mimicking Intramyocellular (IMCL) and Extramyocellular Lipids (EMCL),” *Appl. Magn. Reson.*, vol. 43, no. 3, pp. 451–457, Oct. 2012, doi: 10.1007/s00723-012-0355-4.

[31] A. Antoniou and C. Damianou, “MR relaxation properties of tissue-mimicking phantoms,” *Ultrasonics*, vol. 119, p. 106600, Feb. 2022, doi: 10.1016/j.ultras.2021.106600.

[32] C. S. Poon, J. Szumowski, D. B. Plewes, P. Ashby, and R. M. Henkelman, “Fat/water quantitation and differential relaxation time measurement using chemical shift imaging technique,” *Magn. Reson. Imaging*, vol. 7, no. 4, pp. 369–382, Jul. 1989, doi: 10.1016/0730-725X(89)90486-4.

[33] C. D. G. Hines, H. Yu, A. Shimakawa, C. A. McKenzie, J. H. Brittain, and S. B. Reeder, “T1 Independent, T2* Corrected MRI with Accurate Spectral Modeling for Quantification of Fat: Validation in a Fat-Water-SPIO Phantom,” *J. Magn. Reson. Imaging JMRI*, vol. 30, no. 5, pp. 1215–1222, Nov. 2009, doi: 10.1002/jmri.21957.

[34] K. Fukuzawa *et al.*, “Evaluation of six-point modified dixon and magnetic resonance spectroscopy for fat quantification: a fat–water–iron phantom study,” *Radiol. Phys. Technol.*, vol. 10, no. 3, pp. 349–358, Sep. 2017, doi: 10.1007/s12194-017-0410-9.

[35] C. P. Bernard, G. P. Liney, D. J. Manton, L. W. Turnbull, and C. M. Langton, “Comparison of fat quantification methods: A phantom study at 3.0T,” *J. Magn. Reson. Imaging*, vol. 27, no. 1, pp. 192–197, 2008, doi: 10.1002/jmri.21201.

[36] V. Fritz, P. Martirosian, J. Machann, R. Daniels, and F. Schick, “A comparison of emulsifiers for the formation of oil-in-water emulsions: stability of the emulsions within 9 h after production and MR signal properties,” *Magn. Reson. Mater. Phys. Biol. Med.*, vol. 35, no. 3, pp. 401–410, Jun. 2022, doi: 10.1007/s10334-021-00970-9.

[37] M. L. Johns and K. G. Hollingsworth, “Characterisation of emulsion systems using NMR and MRI,” *Prog. Nucl. Magn. Reson. Spectrosc.*, vol. 50, no. 2, pp. 51–70, Mar. 2007, doi: 10.1016/j.pnmrs.2006.11.001.

[38] G. S. Ioannidis, K. Nikiforaki, G. Kalaitzakis, A. Karantanas, K. Marias, and T. G. Maris, “Inverse Laplace transform and multiexponential fitting analysis of T2 relaxometry data: a phantom study with aqueous and fat containing samples,” *Eur. Radiol. Exp.*, vol. 4, no. 1, p. 28, May 2020, doi: 10.1186/s41747-020-00154-5.

[39] K. Nikiforaki *et al.*, “Multiexponential T2 relaxometry of benign and malignant adipocytic tumours,” *Eur. Radiol. Exp.*, vol. 4, no. 1, p. 45, Aug. 2020, doi: 10.1186/s41747-020-00175-0.

[40] F. Goodarzi and S. Zendehboudi, “A Comprehensive Review on Emulsions and Emulsion Stability in Chemical and Energy Industries,” *Can. J. Chem. Eng.*, vol. 97, no. 1, pp. 281–309, 2019, doi: 10.1002/cjce.23336.

[41] G. Chen and D. Tao, “An experimental study of stability of oil–water emulsion,” *Fuel Process. Technol.*, vol. 86, no. 5, pp. 499–508, Feb. 2005, doi: 10.1016/j.fuproc.2004.03.010.

[42] R. Eötvös, “Ueber den Zusammenhang der Oberflächenspannung der Flüssigkeiten mit ihrem Molecularvolumen,” *Ann. Phys.*, vol. 263, no. 3, pp. 448–459, 1886, doi: 10.1002/andp.18862630309.

[43] S. Sajjadi, “Effect of mixing protocol on formation of fine emulsions,” *Chem. Eng. Sci.*, vol. 61, no. 9, pp. 3009–3017, May 2006, doi: 10.1016/j.ces.2005.10.071.

[44] R. D. Hazlett and R. S. Schechter, “Stability of macroemulsions,” *Colloids Surf.*, vol. 29, no. 1, pp. 53–69, Jan. 1988, doi: 10.1016/0166-6622(88)80171-9.

[45] K. Szymczyk, A. Zdziennicka, and B. Jańczuk, “Effect of Polysorbates on Solids Wettability and Their Adsorption Properties,” *Colloids Interfaces*, vol. 2, no. 3, Art. no. 3, Sep. 2018, doi: 10.3390/colloids2030026.

[46] A. Takamura, T. Minowa, S. Noro, and T. Kubo, “Effects of Tween and Span Group Emulsifiers on the Stability of o/w Emulsions,” *Chem. Pharm. Bull. (Tokyo)*, vol. 27, no. 12, pp. 2921–2926, 1979, doi: 10.1248/cpb.27.2921.

[47] D. J. McClements, “Critical Review of Techniques and Methodologies for Characterization of Emulsion Stability,” *Crit. Rev. Food Sci. Nutr.*, vol. 47, no. 7, pp. 611–49, Oct. 2007.

[48] K.-H. Kim, S. Gohtani, R. Matsuno, and Y. Yamano, “Effects of Oil Droplet and Agar Concentration on Gel Strength and Microstructure of O/W Emulsion Gel,” *J. Texture Stud.*, vol. 30, no. 3, pp. 319–335, 1999, doi: 10.1111/j.1745-4603.1999.tb00220.x.

[49] Y. Yamano, Y. Kagawa, and K.-H. Gohtani, “Stability and Uniformity of Oil Droplets in Preparation of O/W Emulsion Agar Gel”.

[50] C. Washington, “Stability of lipid emulsions for drug delivery,” *Adv. Drug Deliv. Rev.*, vol. 20, no. 2–3, pp. 131–145, Jul. 1996, doi: 10.1016/0169-409X(95)00116-O.

[51] G. Finotello, J. T. Padding, N. G. Deen, A. Jongsma, F. Innings, and J. A. M. Kuipers, “Effect of viscosity on droplet-droplet collisional interaction,” *Phys. Fluids*, vol. 29, no. 6, p. 067102, Jun. 2017, doi: 10.1063/1.4984081.

[52] K. H. Al-Dirawi, K. H. A. Al-Ghaithi, T. C. Sykes, J. R. Castrejón-Pita, and A. E. Bayly, “Inertial stretching separation in binary droplet collisions,” *J. Fluid Mech.*, vol. 927, p. A9, Nov. 2021, doi: 10.1017/jfm.2021.674.

[53] B. Bera, R. Khazal, and K. Schroën, “Coalescence dynamics in oil-in-water emulsions at elevated temperatures,” *Sci. Rep.*, vol. 11, no. 1, Art. no. 1, May 2021, doi: 10.1038/s41598-021-89919-5.

[54] L. Baroudi, S. R. Nagel, J. F. Morris, and T. Lee, “Dynamics of viscous coalescing droplets in a saturated vapor phase,” *Phys. Fluids*, vol. 27, no. 12, p. 121702, Dec. 2015, doi: 10.1063/1.4936942.